https://doi.org/10.5194/egusphere-2026-1039
Preprint. Discussion started: 30 April 2026

Modeling ice rich permafrost landscapes with CLM5 using dynamically coupled tiles

Esther Bender[1], Matvey V. Debolskiy[2], Kjetil Aas[3], Sebastian Westermann[2], Fang Li[4], Jiawen Zhu[4], and Hanna Lee[1]

[1]Department of Biology, Norwegian University of Science and Technology, Trondheim, Norway
[2]University of Oslo, Sem Sælands vei 1, 0316 Oslo, Norway
[3]CICERO - Center for International Climate Research, Oslo, Norway.
[4]State Key Laboratory of Earth System Numerical Modeling and Application, Institute of Atmospheric Physics, Chinese Academy of Sciences, Beijing 100029, China

Correspondence: Esther Bender (esther.bender@ntnu.no)

Abstract. Thawing of extended amount of ground ice in permafrost regions can lead to rapid, large-scale landscape changes known as thermokarst, which significantly alter the thermal, hydrological and biogeochemistry state of the soil and the land surface. These thermokarst processes are driven by excess ground ice and permafrost microtopography. However, large-scale land surface models, used in coupled earth system models for climate predictions, do not represent such small-scale processes, and may therefore miss important mechanism that could contribute to underestimation of current greenhouses emission predictions from the permafrost regions. In this study we implement a new tiling approach in the Community Land Model, version 5.0, which is used in several Earth System Models, which already includes representation of excess ground ice, to resolve permafrost. The approach divides the vegetated land unit of a grid cell in two interacting tiles, that exchange snow, heat, and water, enabling simulation of rapid thaw processes under permafrost degradation. We evaluate this model configurations at two contrasting sites: a palsa mire landscape in northern Norway, and an ice-wedge polygon landscape in northeastern Siberia. The new implementation significantly improves the representation of soil temperature and soil moisture dynamics. It successfully captures the coexistence of two contrasting landscapes, a cold dry elevated higher tile and a warm, saturated lower tile. At the palsa sites, the tiling approach proves to be necessary to maintain stable Palsa conditions until 2014. These results demonstrate that explicitly representing excess ice and landscape dynamics in land surface models improves simulation of permafrost dynamics and may help reduce uncertainty in projections of permafrost-carbon feedbacks.

1 Introduction

Permafrost - defined as ground that remains at or below 0°C for at least two consecutive years - underlies large portions of the Northern Hemisphere and constitutes a key component of the Earth system. Permafrost landscapes exert strong control on Arctic hydrology, ecosystem structure, soil thermal regime, and biogeochemical cycling, and are therefore central to determining the trajectory of Arctic landscape under a changing climate. Permafrost underlies approximately $15\,\%$ of the land area of the Northern Hemisphere (Obu et al., 2019; Ran et al., 2022). Permafrost soils store up to 1400 PgC, roughly twice

https://doi.org/10.5194/egusphere-2026-1039
Preprint. Discussion started: 30 April 2026

the amount currently contained in the atmosphere. The majority of this carbon (Schuur et al., 2015; Hugelius et al., 2014, approximately 1035 PgC) is located within the upper three meters of the soil profile and is therefore vulnerable to mobilization upon permafrost thawing.

In certain regions, permafrost soils contain substantial amounts of ground ice that have accumulated over thousands of years. Cold, continental, paleoclimatic conditions across the high Arctic favored the formation of patterned permafrost landscapes characterized by large syngenetic ice wedges. In the lower and warmer Scandinavian Arctic, the formation and persistence of permafrost depend strongly on small-scale microclimatic, surface, and subsurface conditions (Seppälä, 2011). Variations in microtopography promote localized permafrost occurrence and give rise to features such as palsas - small, elevated peat mounds with frozen, ice-rich cores - and peat plateaus, both of which can contain substantial amounts of ground ice. Temperature-driven melting of excess ground ice is associated with ground subsidence, which can substantially transform landscapes within short timescales (years to decades; Turetsky et al. (2019); Grosse et al. (2013)). This process, known as thermokarst, occurs when large volumes of ground ice melt rapidly, triggering pronounced changes in surface topography, hydrology, and soil thermal regimes. Palsas and ice-wedge polygons - patterned landscapes formed by repeated freeze-thaw cracking and ice-wedge - are among the most prominent thermokarst landforms. Polygon tundra dominates large areas of the carbon-rich continuous permafrost zone and therefore stores vast quantities of permafrost carbon, making it a critical component of the Arctic carbon cycle.

In the polygon tundra, thermokarst commonly drives the transition from low-centered polygons (LCPs) to high-centered polygons (HCPs), while in Fennoscandia, the collapse of palsas represents a prominent thermokarst process. Thermokarst fundamentally alters soil hydrology, snow distribution, soil temperature, and carbon dynamics, thereby influencing both the magnitude and timing of future greenhouse gas emissions from Arctic regions (Liljedahl et al., 2016). Depending on local hydrological conditions, thermokarst can either accelerate or temporarily slow down permafrost degradation. Circumpolar studies indicate that up to 20 % of the northern permafrost is underlain by soil features promoting thermokarst activity (Olefeldt et al., 2016). These ice-rich permafrost landscapes contain up to 50 % of the total permafrost carbon, underscoring their critical role in the permafrost-carbon–climate feedback (Olefeldt et al., 2016).

Earth system models (ESMs) are widely used to project future climate change and associated greenhouse gas emissions, yet they lack an explicit representation of permafrost microtopographic and thermokarst processes. As a result, current ESMs model only gradual thawing due to warming, but omit thermokarst entirely, leading to large uncertainties and a likely underestimation of future carbon emissions. Several synthesis studies and community assessments (Schuur et al., 2022; Turetsky et al., 2019) have emphasized that representing thermokarst processes in ESMs is essential for improving projections of permafrost stability and carbon feedback.

Arctic surface air temperatures have increased roughly four times the global average rate in recent decades (Rantanen et al., 2022), accompanied by widespread permafrost warming (Biskaborn, 2019), and increased thermokarst activity across diverse regions (Runge et al., 2022; Vasiliev et al., 2020; Farquharson et al., 2019). In response, substantial efforts have been made to improve permafrost representation in land surface models. These include advances in peat representation (Chadburn et al., 2022), the incorporation of excess ground ice and thaw induced subsidence (Lee et al., 2014; Ekici et al., 2019) and the use of duplicated soil columns to explore the sensitivity of permafrost thaw to ground-ice content (Cai et al., 2020).

Tiling approaches have been proven particularly effective for representing heterogeneity in permafrost landscapes. Point-scale tiling approaches have been applied successfully in the Noah-MP land surface model (Aas et al., 2019), while Smith et al. (2022) introduced an explicit tiling framework in JULES. In parallel, a representation of excess ice, subsidence and tiling has been implemented in the CryoGrid model and has been used extensively to study thermokarst processes across a range of permafrost landscapes (Westermann et al., 2016; Langer et al., 2016; Nitzbon et al., 2019; Martin et al., 2021; Nitzbon et al., 2021, 2020; Martin et al., 2019). These studies demonstrate that tiling provides a physically consistent means of representing thermokarst-driven landscape heterogeneity.

However, no dynamically coupled tiling approach that explicitly represents permafrost microtopography has yet been implemented in any of the land surface models within the framework of Earth System Modeling. Earth System Models are necessary to fully understand coupled processes and feedbacks within the Earth system. They enable us to get a detailed overview of future Earth system processes and feedbacks. Missing such crucial processes as thermokarst hinders accurate projections of future greenhouse gas emissions.

Here, we present a new implementation of dynamically coupled tiles in the Community Land Model (CLM5) that enables the explicit representation of microtopographic permafrost landscapes and associated thermokarst processes. CLM is a core land component of multiple ESMs (Matthes et al., 2025), including the Community Earth System Model (CESM) and NorESM, and therefore underpins many simulations contributing to IPCC assessments. CLM has demonstrated robust performance in permafrost simulations within CMIP5 and CMIP6 (Burke et al., 2020; Koven et al., 2013) and already includes detailed representations of soil thermal physics, freeze-thaw processes, vertically resolved soil carbon, detailed soil layers, and excess ground ice. When run with its biogeochemical module activated, CLM explicitly simulates carbon, methane, and nitrogen fluxes and storage (Lawrence et al., 2019), making it a powerful tool for projecting future greenhouse gas emissions. The approach captures both gradual permafrost thaw and rapid thaw associated with ground-ice melt and surface subsidence, by implementing lateral exchange of heat, water, and snow between landscape elements. We evaluate model implementation and performance at two contrasting well-observed sites; an ice-wedge polygon tundra on Samoylov Island in northeastern Siberia and a thawing peat plateau-palsa system at Iškoras in northern Fennoscandia. Using a comprehensive set of observations, we assess model performance for soil physics (snow, soil thermal regime, and hydrology). A sensitivity analysis is conducted to quantify the relative importance of snow redistribution, lateral heat fluxes, and lateral water fluxes for permafrost stability.

Accordingly, this study addresses the following research questions

1. Can ice-rich polygonal tundra and peat plateau landscapes in permafrost regions be realistically represented in CLM5 using dynamically coupled tiles?

2. How does the tiling approach influence soil temperature, active layer thickness, and soil moisture dynamics?

3. Which process exerts the strongest control on soil physical conditions and permafrost stability?

https://doi.org/10.5194/egusphere-2026-1039
Preprint. Discussion started: 30 April 2026

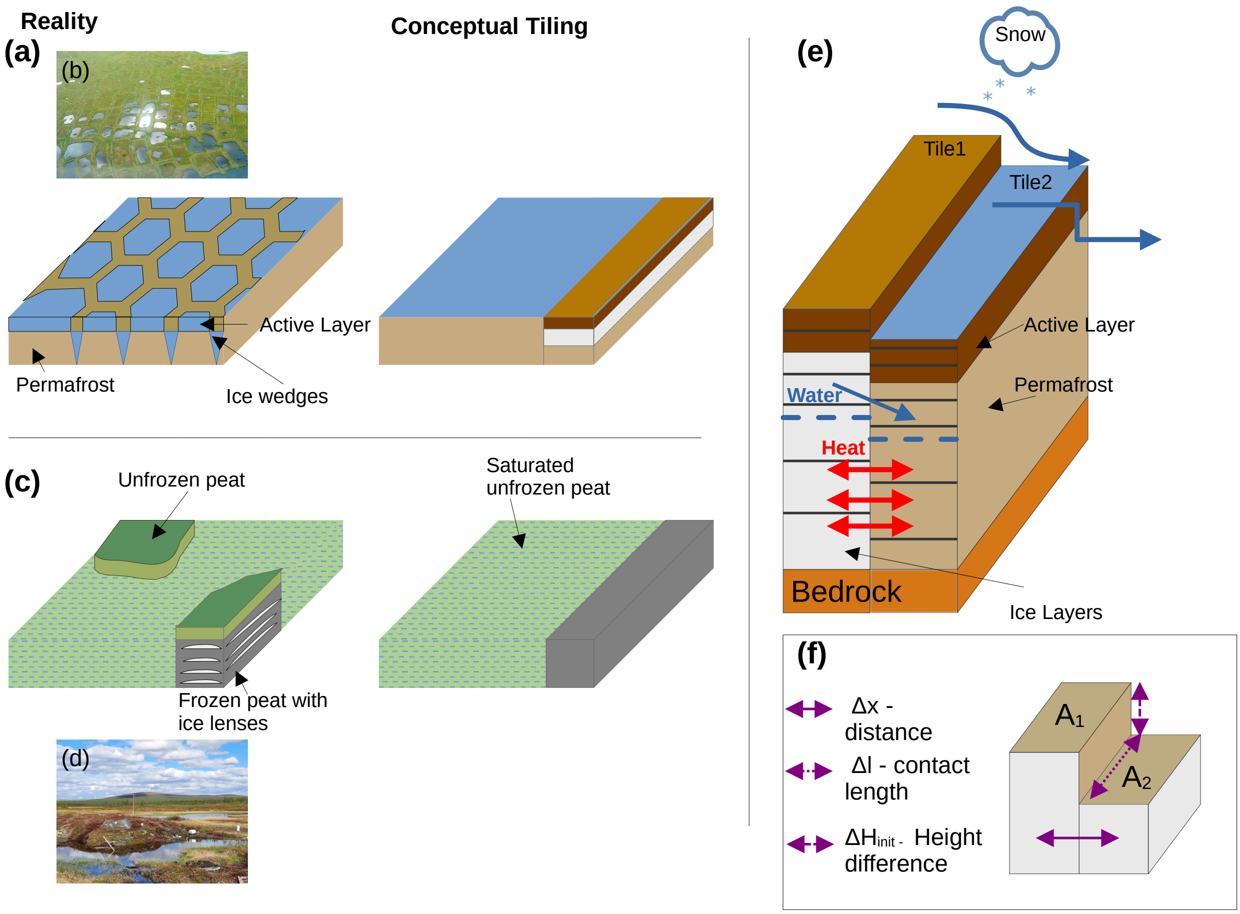

Figure 1. Schematic representation of the modeling approach for the polygon landscape (a) and the peat plateau (c). Panel b shows a picture of a high centered polygon in Samoylov (Fritz et al., 2016) and d) a palsa-mire landscape in Iškoras (© Hanna Lee). Panel e) shows how the tiling is implemented in the model and the lateral fluxes. f) gives an overview of the geometrical parameters used in the model approach.

2 Methods

90 In this study, we implement a tiling approach for permafrost soils in the Community Land Model (CLM5, Version 2.0). To represent microtopography in permafrost landscapes, typical patterned permafrost landscapes are discretized into two dynamically coupled tiles, which exchange lateral fluxes of heat and water, as well as snow redistribution. The height difference between the soil columns is time-dependent, enabling ground subsidence due to the melting of excess ground ice. This approach allows microtopographic evolution to be simulated explicitly. A schematic overview of the modeling approach is shown in Fig. 1.

2.1 Model: CLM5

The Community Land Model version 5 (CLM5) is the land component of the CESM and is widely used to simulate land surface processes at regional to global scales. CLM5 is a process-based model that includes detailed representations of soil thermal and hydrological processes. It includes several processes relevant for permafrost modeling, such as soil and snow hydrology (including subsurface freezing), surface energy, and heat transfer in soil and snow with explicit treatment of phase changes. CLM5 can build up to 12 snow layers. It can be run with up to 54 soil layers, of which the upper 49 are also hydrologically active. The lowermost five soil layers represent bedrock and are not hydrologically active. CLM5 can optionally be run with the biogeochemical model that simulates vertically resolved carbon, nitrogen, and methane pools and fluxes and accounts for vegetation dynamics and land-use change (Lawrence et al., 2019). In its standard configuration, CLM5 does not include lateral exchange of heat or water between grid cells or between sub grid units such as columns or patches, except for river routing.

Within a CLM5 grid cell, multiple landscape types (lake, urban, crop, glacier and natural vegetated landscapes) can coexist, with each landscape type represented by one or more separate columns. The natural vegetated landunit has a single column which may include multiple patches corresponding to different plant functional types. In standard CLM5, all natural vegetated landscapes patches within a grid cell share a single soil column and therefore identical soil stratigraphy and properties. This limitation prevents an explicit representation of microtopography, which requires distinct soil columns within the same natural vegetated land unit. To overcome this limitation, the natural vegetated soil column is subdivided into two tiles. These tiles represent a new sub grid hierarchy that allows two distinct natural vegetated soil columns with different soil stratigraphy and state variables to coexist within a single grid cell. Figure 1 illustrates the tiling concept, the implemented lateral fluxes, and the associated geometrical parameters.

2.1.1 Geometrical parameters and tiling

To represent microtopography in permafrost regions, the natural vegetated column is divided into two tiles following Smith et al. (2022). New time-independent parameters are introduced: the characteristic area of the two tiles – A_1, A_2 (m), the characteristic horizontal distance between tiles – dx (m) the length of the contact interface between tiles – dl (m), and the initial height difference between the tiles – ΔH_{init} (m). These parameters correspond to A_1, A_2, Δx, Δl and Δz in Smith et al. (2022). Parameter values for the Samoylov and Iškoras sites are adopted from Table 2 in Smith et al. (2022). In addition, a new parameter f_{split} $(-)$ is introduced to control the initial partitioning of excess ground ice between the two tiles. The total amount of excess ice prescribed for a grid cell, obtained from the "Circum- Arctic map of Permafrost and Ground-ice Conditions" (Brown et al., 1997) is multiplied by f_{split} and $(1 - f_{split})$ for tile 1 and tile 2, respectively. The values of f_{split} are 0.7 for Samoylov and 0.99 for Iškoras. An overview of the parameter values can be found in Table 1.

2.1.2 Excess ice

CLM5 is equipped with an excess ice parametrization based on Lee et al. (2014). Excess ice represents ground ice volumes that exceed the pore space of the soil matrix. In grid cells containing excess ice, the prescribed ice volume is evenly distributed

	Iškoras	Samoylov
A_1	25.0	70.0
A_2	25.0	58.0
dx	2.0	2.1
dl	5.0	26.7
ΔH_{init}	0.68	0.38
f_{split}	0.99	0.7

Table 1. Geometrical parameters for Iškoras and Samoylov

across the soil layers between the active layer depths and the bedrock by increasing the thickness of the affected soil layers. The additional volume consists of frozen water.

The presence of excess ice modifies soil thermal properties, in particular soil thermal conductivity. Upon melting, excess ice reduces soil layer thickness and induces vertical ground subsidence. Meltwater released from excess ice contributes to soil moisture and affects subsurface hydrology. A detailed description of the excess ice formulation is provided in Lee et al. (2014), with further adaptation in Cai et al. (2020).

2.1.3 Snow redistribution

Snow redistribution follows the approach of Aas et al. (2019) and Smith et al. (2022). To simulate the effect of windblown snow, freshly fallen snow is redistributed from the upper to the lower tile until the snow depth of the lower tile exceeds the current height difference between the tiles (Equation 1). The current height difference between tiles ΔH_t, is calculated at each time step by accounting for the initial height difference ΔH_{init}, subsidence due to melting of excess ice, and the current snow depth, following:

$$\begin{aligned} \Delta H^t_{soil} &= \Delta H_{init} - \Delta z^t_{exice,k=1} + \Delta z^t_{exice,k=2} \quad \text{for } S \le 0 \\ \Delta H^t_{soil} &= \Delta H_{init} - \Delta z^t_{exice,k=1} + \Delta z^t_{exice,k=2} + S_{k=1} - S_{k=2} \quad \text{for } S > 0 \end{aligned} \tag{1}$$

Here, $k = 1,2$ denotes the tile index, ΔH_{init} is the initial height difference (m), S is the current snow depth (m), $\Delta z^t_{exice,k}$ is cumulative subsidence at time t for k^{th} tile, calculated as:

$$\Delta z^t_{exice,k} = \left(\sum_{n=1}^{N} w^t_{exice,i} - \sum_{n=1}^{N} w^{t=0}_{exice,i} \right) \rho_{ice}^{-1} \tag{2}$$

where $w^t_{exice,i}$ is the areal density of excess ground ice in the i^{th} soil layer (kg m^{-2}) and ρ_{ice} is the volumetric mass density of ice (kg m^{-3}). If ΔH^t_{soil} is positive, tile 1 is higher than tile 2.

To represent snow trapping by vegetation a threshold (v of $0.05\,\mathrm{m}$) is introduced. No snow redistribution occurs below this threshold. If the snow depth exceeds v snow is redistributed from the higher tile to the lower tile. The redistributed snow depth

https://doi.org/10.5194/egusphere-2026-1039
Preprint. Discussion started: 30 April 2026

is scaled by the relative areas of the tiles:

$$\begin{aligned}
&S^{t=0}_{k=1} = S^{t=-1}_{k=1} + 0 && \text{,for}: \Delta H^{t}_{soil} > 0 \quad \text{and} \quad S_1 > v \\
&S^{t=0}_{k=2} = S^{t=-1}_{k=2} + S^{t=0}_{k=2} + S^{t=0}_{k=1} \cdot \frac{A_1}{A_2} && \text{,for}: \Delta H^{t}_{soil} > 0 \quad \text{and} \quad S_1 > v \\
&S^{t=0}_{k=2} = S^{t=-1}_{k=2} + 0 && \text{for}: \Delta H^{t}_{soil} < 0 \quad \text{and} \quad S_2 > v \\
&S^{t=0}_{k=1} = S^{t=-1}_{k=1} + S^{t=0}_{k=1} + S^{t=0}_{k=2} \cdot \frac{A_2}{A_1} && \text{for}: \Delta H^{t}_{soil} < 0 \quad \text{and} \quad S_2 > v
\end{aligned} \tag{3}$$

with $S^{t=0}$ denoting the additional snow depth at the current timestep and $S^{t=-1}$ the snow depth from the previous timestep, A is the tile area.

2.1.4 Lateral heat fluxes

The subsurface lateral heat flux between the tiles is implemented, following Aas et al. (2019) and Smith et al. (2022). For each soil layer, the overlapping portion between the soil column of tile 1 and the corresponding layer of tile 2 is determined by accounting for the current height difference (Eq. 1, without snow) and differences in soil layer thickness between the tiles. The lateral heat flux through the overlapping portion of two adjacent soil layers is calculated as:

$$q_{1,2} = k_{sat} \cdot \frac{T_1 - T_2}{dx} \cdot \Delta O_{soil} \cdot \frac{dl}{A_{1,2}} \tag{4}$$

where k_{sat} is the thermal conductivity of the layers' interface, T_1 and T_2 are the temperatures of the corresponding soil layers of tile 1 and 2, ΔO_{soil} is the thickness of the overlapping soil layer portion.

Heat fluxes are calculated for each soil layer individually after vertical heat fluxes, and phase change processes are resolved. The total lateral heat flux into or out of each tile is obtained by summing the individual fluxes over all thermally active soil layers.

2.1.5 Lateral water fluxes

A lateral subsurface water flux between the tiles is implemented based on differences in the height of the perched water table. Water flows from the tile with the higher perched water table to the tile with the lower one. If perched water is present, the relative depths of the perch water tables are calculated with respect to the opposing tile. The inflow of water to the receiving tile, Q_{flx}, is calculated as:

$$\begin{aligned}
&Q_{flx} = \left| \cdot \left(\sum_{k_{frost}}^{k_{perch}} * \cdot h_{ksat} \cdot \Delta z_k \right) \cdot dl \cdot H_g \right| \\
&H_g = P_{k=1} - (P_{k=2} + \Delta H^{t}_{soil})
\end{aligned} \tag{5}$$

where k_{frost} denotes the soil layer of the frost table, k_{perch} the soil layer of the perch water table of the receiving tile, h_{ksat} the saturated hydraulic conductivity of layer k, Δz_k the thickness of the soil layer k, dl the contact length between tiles, and H_g

https://doi.org/10.5194/egusphere-2026-1039
Preprint. Discussion started: 30 April 2026

the heat gradient. The heat gradient is calculated from the difference between the depth of the perch water table of tile 1 ($P_{k=1}$) and tile 2 ($P_{k=2}$) and the current height difference between tiles ΔH^{t}_{soil}. Lateral water fluxes are calculated before updating the perch water table depth and are included in the subsequent recalculation of the perched water table. Vertical percolation within the receiving tile is computed after the lateral water flux.

To prevent excess ice surface water accumulation on the lower tile, an additional land overflow mechanism is implemented. If the depth of the standing surface water on the lower tile exceeds ΔH^{t}_{soil}, excess water is added to the land overflow and removed from the grid cell as surface runoff.

2.2 Site description

To evaluate the performance of the implemented tiling approach, two study sites representing vulnerable patterned permafrost landscapes are selected.

2.2.1 Samoylov

Samoylov Island (72 °22 'N, 126°28'E) is an island in the Lena River delta in northern Siberia, Russia. The site is located in the zone of cold continuous permafrost zones, with a mean annual ground temperature of approximately -9°C, (Boike et al., 2019). The landscape is characterized by ice-wedge polygons and water bodies of various sizes, spanning polygon degradation stages from intact low centered polygons to the higher terrain, thaw ponds closer to the river (Nitzbon et al., 2019). Vegetation consists primarily of lowland tundra species.

The Samoylov region has been intensely studied over the past two decades, including investigations of carbon cycling (Knoblauch et al., 2013, 2018), and surface energy balance (Langer et al., 2011a, b). The site is equipped with meteorological instruments and an eddy-covariance flux tower. Long-term soil and meteorological observations are available (Boike et al., 2019, 2013), and the site has been widely used for permafrost model evaluation and Earth system model validation (Aas et al., 2019; Chadburn et al., 2017; Ekici et al., 2019; Nitzbon et al., 2021).

The polygon landscape is represented by two tiles: an elevated polygon Rim containing 70 % of the excess ground ice and a lower polygon center containing the remaining excess ice (Fig. 1 a, b, e).

2.2.2 Iškoras

Iškoras (69 °30'N, 25°24'E) is a site located in northern Norway, at an elevation of approximately 399 m a.s.l.. The site is situated in the sporadic permafrost zone and is characterized by palsas (permafrost affected peat plateaus) embedded in a surrounding permafrost-free mire. The palsas are in various states of degradation, ranging from intact features to collapsed structures forming thaw ponds (Pirk et al., 2024; Jiao et al., 2023).

The site has been intensively studied since 2017 and is representative of degrading peat plateaus. Meteorological forcing is obtained from the nearby Karasjok weather station, which provides temperature and precipitation records dating back to 1901. In addition, eddy-covariance measurements and observations of soil temperature, soil moisture, and carbon fluxes for both palsa and mire environments are available. The site has previously been used for Earth system model evaluation (Smith et al., 2022).

Using the tiling approach, the site is represented by two tiles: a Palsa tile containing excess ice and a permafrost-free Mire tile (Fig.1 c, d, e).

2.3 Forcing data

The model is forced using data from the Global Soil Wetness Project Phase 3 dataset GSWP3, (Dirmeyer et al., 2006) at a temporal resolution of 3 hours. Site-specific forcing data are extracted from the global dataset and bias corrected using available observational data.

At Iškoras, observational data from the Karasjok weather station (Norwegian Meteorological Institute, 2024) are used for air temperature and precipitation. This station is used instead of the Iškoras weather station, because the latter is located on the summit of the Iškoras mountain at an elevation exceeding $500\,\mathrm{m}$ a.s.l., whereas the peat plateau represented in the model is located in a relatively flat terrain. Although winter cold extremes at Karasjok may not always occur at Iškoras, the Karasjok data provide the most representative forcing for the modeled landscape. Daily differences in air temperature and precipitation between GSWP3 and observations are calculated for 1901-2014. These differences are added to the GSWP3 data set. No additional bias correction is applied.

At Samoylov, mean daily air temperature differences between observations from the Samoylov meteorological station (Boike et al., 2022) and GSWP3 are calculated for the period 2002-2014 and added to each corresponding day of the year for the forcing data set. For precipitation, the mean percentile difference between observations and GSWP3 for liquid summer precipitation is calculated, and GSWP3 precipitation is reduced accordingly. In addition, winter precipitation is reduced by $25\,\%$. Reliable winter precipitation measurements are not available for Samoylov, and satellite-based products are known to overestimate precipitation at this site, which generally exhibits a dry climate. The resulting mean annual precipitation for the forcing data is $236\,\mathrm{mm\,year^{-1}}$, with mean annual liquid precipitation of $117\,\mathrm{mm\,year^{-1}}$, which is slightly lower but comparable to the observed $146\,\mathrm{mm\,year^{-1}}$ (Boike et al., 2022).

2.4 Model set up

To improve the representation of the study sites, several standard model parameters and surface properties are modified. The soil column is initialized with a total depth of $54\,\mathrm{m}$ and consists of 54 soil layers. The upper 49 soil layers, extending to a depth of $10\,\mathrm{m}$ are hydrologically active. Individual soil layer thicknesses range from 0.05 near the surface to $0.30\,\mathrm{m}$ at depth. The lowermost five layers represent bedrock and are each $10\,\mathrm{m}$ thick. Soil texture is prescribed for each modeling site. In CLM5, mineral soil properties are defined by fractions of sand and clay, while organic matter can be added to individual soil layers. Organic carbon density of $130\,\mathrm{kg\,m^{-3}}$ is used to represent peat. The fractions of sand, clay, and organic matter determine soil thermal and hydraulic parameters.

At Iškoras, soil composition is similar for both tiles. Tile 1 has a $1.5\,\mathrm{m}$ thick peat layer on the surface with organic carbon density of $130\,\mathrm{kg\,m^{-3}}$, underlain by sandy mineral soil. Tile 2 has a slightly shallower peat layer. A detailed description of

https://doi.org/10.5194/egusphere-2026-1039
Preprint. Discussion started: 30 April 2026

		Lateral fluxes		
experiment name	two tiles	Snow redistribution	heat flux	water flux
REF	no	no	no	no
coupled	yes	yes	yes	yes
no flux	yes	no	no	no
+ S	yes	yes	no	no
+ H	yes	no	yes	no
+ W	yes	no	no	yes
+ WH	yes	no	yes	yes
+ SW	yes	Yes	no	yes
+ SH	yes	yes	yes	no

Table 2. Name and description of the experiments performed in the sensitivity study, S in the Name stands for Snow redistribution, H for lateral heat flux and W for lateral water flux

the soil layer structure is provided in Appendix Table A1. The maximum saturated area fraction is set to 75 % and the mean topographic slope is set app. 6°, representing a relatively flat landscape.

At Samoylov tile 1 is initialized with a shallow peat layer and sandy-clay (60 % sand). Tile 2 contains a substantially thicker peat layer and a more clay-rich mineral soil at depth. The maximum saturated area fraction is set to 95 % and the mean slope is again set to 6°.

For both study sites, cold start soil temperatures are initialized at -2°C, which allows the mire at Iškoras to thaw within a realistic timescale while maintaining permafrost conditions. Initial soil moisture is set to near saturated conditions (95 % saturation).

The snow accumulation factor k_{acc} is set to 0.4, resulting in a rapid buildup of a closed snow cover of the grid cell. This choice reflects the relatively small and flat landscapes considered, which tend to be either fully snow covered or snow free. The snow covered fraction of a grid cell, indicates what percentage of a grid cell is covered with snow and is used as an indicator of snow cover. No adjustments are made to snowmelt parameters.

All columns are covered with the plant functional type of arctic grass. All simulations are conducted in satellite-Phenology mode, without activating biogeochemistry and predefined vegetation properties. This means that there is no carbon cycling and vegetation properties are predefined. The model is spun up for 150 years using meteorological forcing from the period 1930-1950 and a pre-industrial atmospheric CO_2 concentration of 284 ppm. The spin-up duration is sufficient for soil physical processes, as deep soil temperature variation was less than 0.05°C at the end of the spin up. Transient simulations (1901-2014) were conducted for the Iškoras and Samoylov sites to evaluate the tiling approach.

https://doi.org/10.5194/egusphere-2026-1039
Preprint. Discussion started: 30 April 2026

2.5 Sensitivity study

To assess the influence of individual processes introduced by the tiling approach- snow redistribution, lateral heat flux, and lateral water flux- a sensitivity study is conducted in which these processes are selectively enabled or disabled. Table 2 summarizes the experiments and their naming convention. The sensitivity experiments are used to quantify the impact of individual processes on soil temperature, soil hydrology, and lateral fluxes, and to identify which processes are required to achieve realistic simulations of patterned permafrost landscapes. At Iškoras all sensitivity simulations are initialized from the spin-up state of the fully coupled tiling configuration. As a result, all experiments except the reference simulation (REF) start with an initial subsidence of $0.08\,\mathrm{m}$. At Samoylov, sensitivity simulations are initialized from the spin up of the REF simulation. Consequently, all simulations start with an elevation of $0.38\,\mathrm{m}$, and do not include prior subsidence due to excess ice loss.

3 Results

Results from the tiling configuration are compared with a standard simulation (hereafter REF) using identical soil parameters and forcing data. Where available, simulations are evaluated against observations. The analysis focuses on snow (section 3.1), that controls the soil thermal regime (section 3.2) and hydrology (section 3.3), as well as excess ice (section 3.4) and lateral heat and water fluxes (3.5). Section 3.6 presents the sensitivity analysis.

3.1 Snow

Snow strongly controls the permafrost thermal regime and distribution; snow redistribution is also a central element of the tiling approach. Figure 2 shows mean daily snow height for Samoylov (a) and Iškoras (b) (2002-2004).

At Iškoras, tiling produces thicker snow cover in the Mire and thinner snow cover at the Palsa. For 2002-2014, maximum end-of-season snow depths (SD) range from $0.18\,\mathrm{m}$ to $0.54\,\mathrm{m}$ on the Palsa and $0.65\,\mathrm{m}$ to $1.09\,\mathrm{m}$ in the Mire. Observations from 2018-2019 (shown in Fig. 2) report SD of $0.18\,\mathrm{m}$ ($0.18\,\mathrm{m}$) at the Palsa and $0.89\,\mathrm{m}$ ($0.73\,\mathrm{m}$) in the Mire, indicating realistic magnitude and spatial contrast.

Snow ablation, defined as the first day in spring when snow depth is zero, occurs between late April and late May, with melt-out on the Palsa about 10 days earlier than in the Mire. REF melt timing lies between both tiles and is approximately 4 days earlier than in the Mire. The significant 10-day difference between Palsa and Mire introduced by tiling is a key driver of subsequent soil-temperature differences (section 3.2) and agrees better with observations.

At Samoylov, snow remains deeper at the Center than at the Rim, while REF falls between both regimes. SD ranges from $0.30\,\mathrm{m}$ to $0.81\,\mathrm{m}$ for the Rim and $0.68\,\mathrm{m}$ - $1.17\,\mathrm{m}$ for the Center(see Fig. 2a). REF shows snow height between $0.39\,\mathrm{m}$ and $0.92\,\mathrm{m}$. Observed SD ($0.09 - 0.71\,\mathrm{m}$), indicates a positive bias in all simulations. This bias likely reflects forcing uncertainties and the absence of wind-driven snow removal, an important process in the Lena River delta. Additionally, disabling wind compaction of snow increased SD by approximately $0.10\,\mathrm{m}$.

Snow onset occurs simultaneously across simulations because redistribution begins only once snow exceeds $0.05\,\mathrm{m}$. Melt-out occurs between late May and late June, with the Rim melting approximately 6 days earlier than the Center and 2 days earlier than REF, consistent with observed timing.

The snow cover fraction (SCF) differs markedly between tiles: the Center remains nearly fully snow-covered throughout winter, whereas the Rim is partially snow covered for extended periods (not shown). This behavior matches aerial observations (Boike et al., 2019, 2013).

Overall, tiling generates two physically consistent snow regimes: thick, continuous snow cover at the Center/Mire, and thinner, spatially variable snow cover at the Palsa/Rim. Despite an overall snow bias at Samoylov, spatial contrasts are realistically represented.

3.2 Ground thermal regime

3.2.1 Soil temperature

At Iškoras, mean annual soil temperatures show clearly separate patterns for Palsa, Mire, and REF. Figure 3 shows mean annual soil temperature at Iškoras from 1901-2014 for the REF simulation (a), Palsa (b), and Mire (c). In the upper $3\,\mathrm{m}$, the Mire is approximately 3°C warmer than the Palsa and slightly warmer than REF. The Palsa remains below 0°C and maintains a stable ALT of around $1\,\mathrm{m}$ for most of the simulated period. Although Palsa soil temperatures increase after 1980, permafrost persists. In contrast, REF exhibits strong warming after 1980, resulting in rapid thaw and loss of Palsa-like conditions. The Mire also shows substantial warming after 1980.

Seasonal differences (Fig. 2 f and g) are dominated by winter processes. Summer temperatures are similar across simulations, whereas winter temperatures diverge strongly. At $0.1\,\mathrm{m}$, winter soil temperatures reach $-10°\mathrm{C}$ at the Palsa but remain only slightly below freezing in the Mire and REF. These differences arise from snow insulation: thick snow cover maintains near-zero temperatures in the Mire, while thin snow cover allows deep penetration of cold winter air. At $0.65\,\mathrm{m}$ depth (approximately the height of the Palsa), temperature differences between Mire and Palsa are reduced, and lateral heat exchange between tiles moderates extremes. The annual temperature amplitude is small for both Palsa and Mire, as most of the energy is used for phase change processes. Comparison with observations shows that modeled soil temperature for the Mire is in good agreement (Fig. 2f), while Palsa temperatures are underestimated in winter and overestimated in summer.

Deep soil temperatures further indicate permafrost state (Figure (A2 a) 2002 to 2014). At the surface, the Mire is approximately 3.3°C warmer than the Palsa and slightly warmer than REF. Below $4\,\mathrm{m}$, REF becomes warmer than the Mire. Surface temperatures remain near 0° C at the Palsa, whereas in the Mire they are above freezing, indicating that permafrost persists only in the Palsa. Below $10\,\mathrm{m}$, differences vanish, reflecting mineral bedrock layers unaffected by tiling.

The depth at which the annual temperature amplitude falls below 1°C is $7.5\,\mathrm{m}$ for the Palsa, $3\,\mathrm{m}$ for the Mire, and $2.3\,\mathrm{m}$ for REF. The thick peat layer at Iškoras provides strong thermal insulation, reducing temperature amplitude with depth. Ongoing thawing in the Mire and REF consumes much of the available energy via phase change rather than warming. Since 1910,

https://doi.org/10.5194/egusphere-2026-1039
Preprint. Discussion started: 30 April 2026

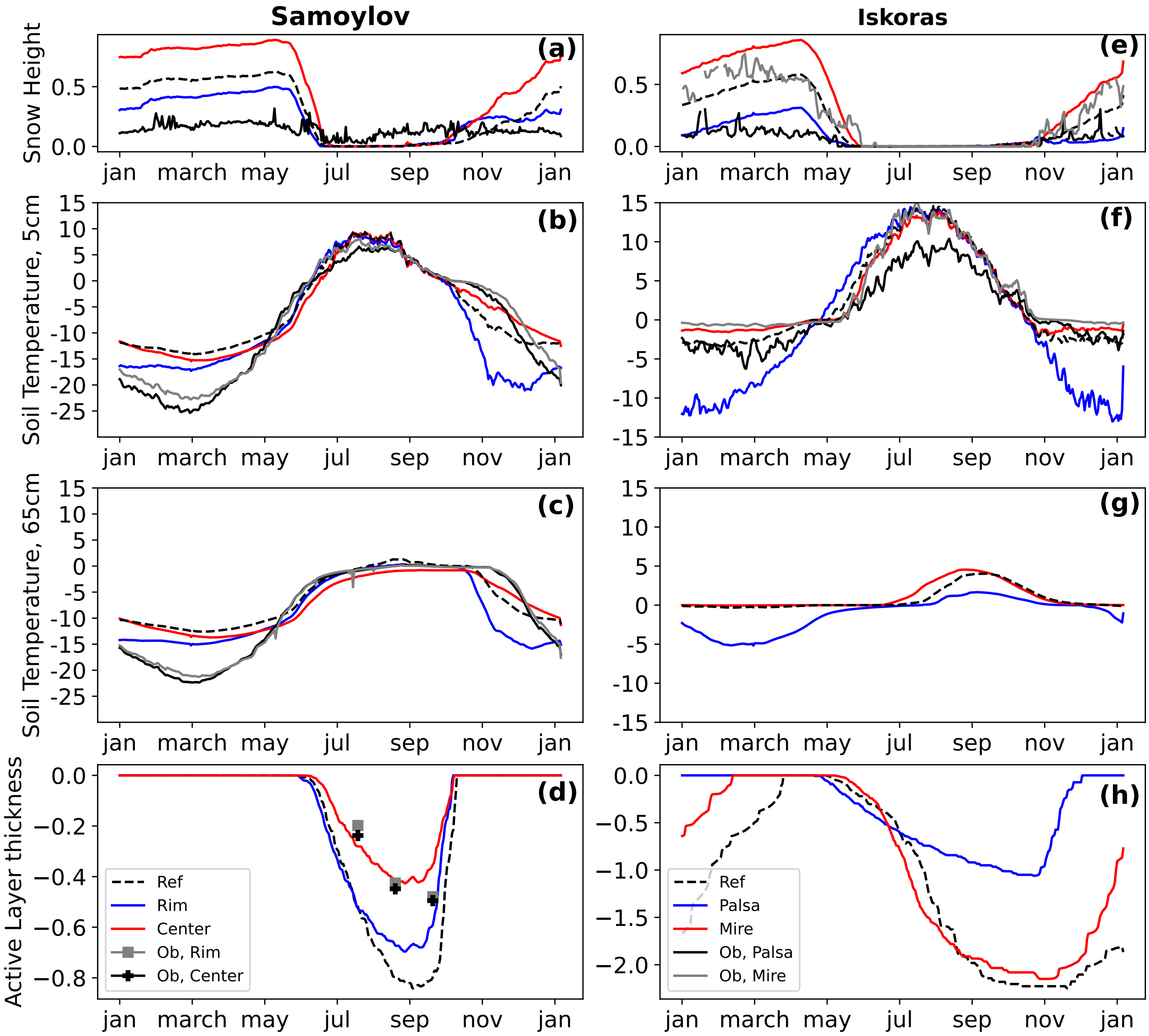

Figure 2. Mean daily (2002-2014) snow height (a, e), surface temperature (b, f), 0.65 m soil temperature (c, d) and Active layer thickness (d, h) for Iškoras (right) and Samoylov (left). Where available observations are shown for comparison. Snow height at Iškoras are form 2018-2019 and soil temperatures for year 2021-2023. For Samoylov snow height measurements don't differ between Rim and Center

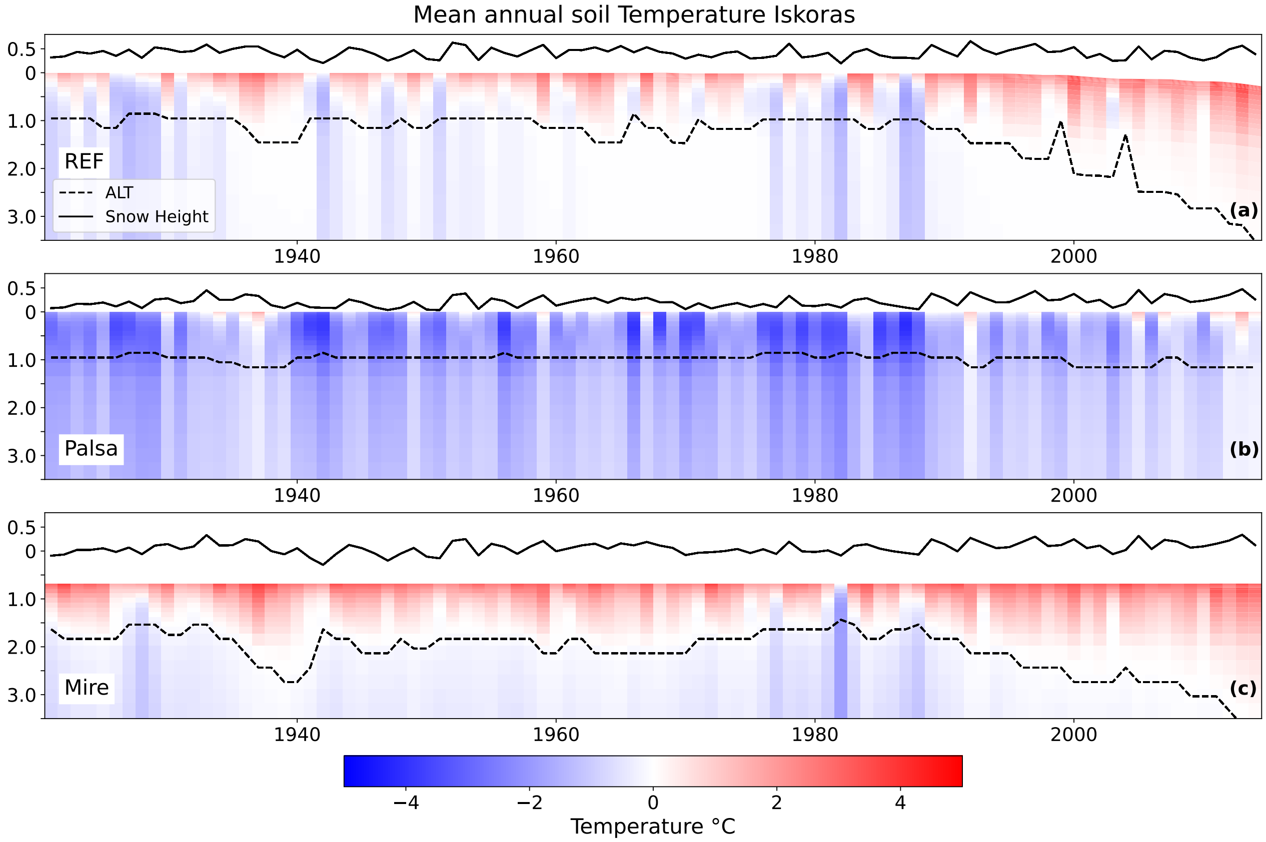

Figure 3. Mean annual soil temperature from 1901-2014 in Iškoras for REF (a), Palsa (b), and Mire (c). Solid lines indicate maximum annual snow height and dashed lines indicate maximum annual ALT.

surface soil temperatures have increased by 2.3° in the Palsa and REF and 1.0° in the Mire. Deep soil temperatures remain stable (Fig. A2 c).

At Samoylov (Fig. 2, left shows soil temperature at 0.10 (b) and 0.65 m (c) depth for Rim, Center, and REF, compared to observations), the Rim shows the largest annual temperature amplitude and the Center the smallest. Summer temperatures are comparable across tiles, but winter temperatures at the Rim are several degrees colder due to reduced snow insulation. However, simulated winter minima remain too warm, relative to observations (modeled -15°C, observed -25°C), primarily because of excessive snow depth. Test simulations with reduced winter precipitation decreased winter soil temperature by 10°C, improving agreement for the Center but producing unrealistically cold Rim temperatures (not shown).

During the freezing period, temperature differences are largest and controlled by soil moisture, which modulates latent-heat consumption during freezing. Tiling improves the freezing-period representation at the Center, whereas Rim temperatures drop too rapidly, likely reflecting faster drying of the Rim in the model than observed.

https://doi.org/10.5194/egusphere-2026-1039
Preprint. Discussion started: 30 April 2026

Mean annual temperature profiles show that tiling improves deep-soil representation (Fig. A2 c). Temperature contrast persists down to the bedrock at $10\,\mathrm{m}$ depth, and tiling reduces the deep-soil warm bias by $1.7°\mathrm{C}$ and better reproduces observed vertical gradients. The depth where the annual temperature amplitude falls below $1°\mathrm{C}$ is approximately $10.15\,\mathrm{m}$ for Rim, Center, and REF, consistent with observations.

Since 1910, soil temperatures at Samoylov have increased. Below $1\,\mathrm{m}$, warming is similar for Rim and Center (around $2°\mathrm{C}$), while surface warming is stronger at the Rim ($3.0°$) than the Center ($2.8°\mathrm{C}$), likely due to drier Rim soils absorbing more summer radiation. REF shows less pronounced warming in the upper $10\,\mathrm{m}$ ($2.7°\mathrm{C}$ warming) but stronger warming at depth ($2.4°\mathrm{C}$).The uniform warming throughout the soil column at REF reflects the lack of lateral heat exchange or ice melting; hence warming only occurs due to an increase in air temperatures from the top.

In summary tiling substantially improves soil-temperature dynamics at both sites, particularly during winter when snow-soil interactions govern permafrost stability.

3.2.2 Active layer

The active layer thickness (ALT) - the soil layer that thaws and refreezes annually - provides an integrated measure of permafrost response. Figure 2 shows mean daily ALT at Samoylov (d) and Iškoras (h).

At Samoylov, REF simulates a September ALT of $0.85\,\mathrm{m}$, whereas tiling yields $0.7\,\mathrm{m}$ at the Rim and $0.44\,\mathrm{m}$ at the Center. Observation values of $0.47\,\mathrm{m}$ (Rim) and $0.49\,\mathrm{m}$ (Center) are closely matched at the Center and substantially better represented overall than REF. ALT at the Rim is approximately $0.2\,\mathrm{meter}$ too deep. This could be a result of (i) ALT measurements being mainly taken in early September, before maximum depth is reached; (ii) observations distinguishing Rim and ice-wedge, whereas the model represents a combined Rim/ice-wedge tile; and (iii) winter soil temperatures that are too warm in the model (section 3.2). Tiling also reproduces the observed seasonal deepening of the active layer from July to September. Since 1901, maximum ALT has deepened by $0.18\,\mathrm{m}$ in REF and at the Rim, but only by $0.1\,\mathrm{m}$ in the Center.

At Iškoras, the Palsa reaches a maximum ALT of $1.05\,\mathrm{m}$. The Mire reaches $2.3\,\mathrm{m}$, compared to $2.5\,\mathrm{m}$ for REF. The persistence of permafrost in the modeled Mire, which is not observed in reality, suggests that thermal insulation of wet peat may be overestimated. Additional cold spells in the forcing data, which are not realistic in Iškoras, lead to too cold winter temperatures and permafrost persistence.

Since 1910 (Fig.3), REF shows $1.4\,\mathrm{m}$ ALT deepening, whereas the Palsa deepens by only $0.2\,\mathrm{m}$. In REF, excess ice melt after 1980 triggers subsidence, surface wetting, rapid warming, and accelerated thaw. Hence, the Palsa-like structure begins to collapse after 1980. Tiling prevents this collapse and maintains Palsa stability throughout the 20th century. While Borge et al. (2017) reported a loss of Palsa area from 1950-2015, some smaller Palsa structures have remained stable until recently. As the model setup resembles a small, stable Palsa structure, these results are still realistic. In general, tiling leads to the development of two different ALT trajectories for the different tiles, significantly improving active-layer modeling.

3.3 Water balance

3.3.1 Soil moisture

Accurate representation of soil moisture and surface water is crucial for carbon-cycle modeling and motivated the implementation of a tiling approach. Simulations were initialized with $95\,\%$ soil saturation, but during spin-up and the 20th century, the Rim at Samoylov and the Palsa at Iškoras dried. Figure 4 shows mean annual volumetric soil moisture from 1980 to 2014.

At Samoylov, the Rim remains drier (0.2 at the surface, 0.4 at depth), while the Center is saturated ($\geq$ 0.9 in the top $0.15\,\mathrm{m}$, approximately 0.8 below). Towards the end of the simulation, the Rim becomes slightly wetter due to warmer soils and a deeper water table. At $1.75\,\mathrm{m}$ depth, both Rim and Center approach the maximum water-holding capacity (0.36) of the mineral soil at depth. The tiling approach thus reproduces distinct soil moisture regimes: a dry Rim and a saturated Center, whereas REF produces a thin saturated surface over drier, deeper soils.

Figure 5 shows summer liquid soil water content at Samoylov for Rim (a), Center (b) and REF (c), compared to observations at Rim (d) and Center (e). The tiling approach closely matches observations, with only small discrepancies near the surface (Fig. 5 f) and improves upon REF. Below $1.0\,\mathrm{m}$, soil water remains frozen.

At Iškoras (Fig. 4 right) tiling produces a clear contrast: the Palsa is dry at the surface and moderately dry throughout the active layer, with increased moisture where excess ice remains; the Mire is saturated to $1.2\,\mathrm{m}$, corresponding to the peat layer thickness. Below this, both Mire and Palsa reach 0.35 , the maximum water-holding capacity of the mineral soil. These moisture regimes persist throughout the simulations, stabilizing the Palsa. REF behaves differently: prior to 1995, surface soils are dry; thereafter, deepening ALT and subsidence increased soil moisture and formed a surface pond. Subsurface wetting in REF is driven by subsidence rather than ALT deepening alone (Andresen et al., 2020).

Observed volumetric water contents confirm realistic Palsa and Mire conditions (Fig. A3). Overall, tiling reproduces contrasting hydrological regimes at both sites, while REF fails to capture the observed soil moisture regime.

3.3.2 Surface water

Surface water forms when snowmelt or rainfall exceeds infiltration or when soils are saturated. Surface water is indicated by solid lines in Fig. 4 and Fig. 5.

At Samoylov, surface water occurs mainly at the Center after snowmelt, peaking in July-August (Fig.5 c), covering $60\,\%$ of the area with water depths up to $0.25\,\mathrm{m}$. No surface water forms on the Rim. In the REF, surface water peaks in August, with $40\,\%$ coverage and shallower depths $(0.15\,\mathrm{m})$. Surface-water patterns have remained relatively stable since 1910 (Fig.4).

A perched water table develops above frozen soil at the Rim, Center, and REF during summer, facilitating lateral water exchange.

At Iškoras, surface water appears in the Mire (Fig. 4) after snowmelt, peaking in July, covering $50\,\%$ of the area, with $0.25\,\mathrm{m}$ water depths. Both water depth and extent increased from 1910 to 2014, eventually forming a permanent pond. No surface water forms at the Palsa. REF initially shows no surface water, but ice melt, and subsidence eventually produces a pond that covers $30\,\%$ of the area with depths of $0.10\,\mathrm{m}$. REF surface water is shallower than in the Mire because the same amount of

https://doi.org/10.5194/egusphere-2026-1039
Preprint. Discussion started: 30 April 2026

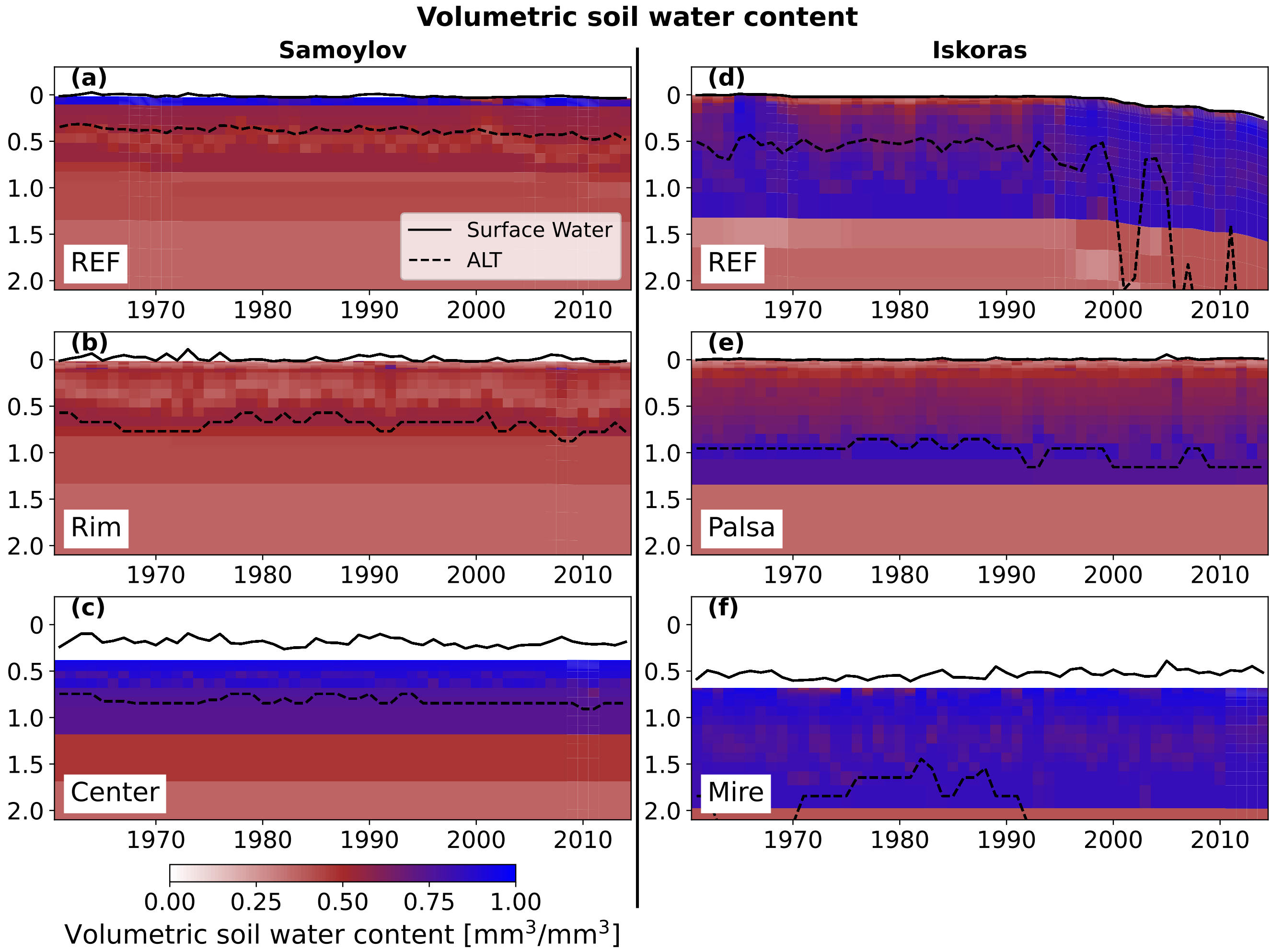

Figure 4. Mean yearly volumetric soil water content at Samoylov (left) and Iškoras (right). Mean values from 1960-2014 are shown for REF(a, d), Rim (Samoylov, b), Center (Samoylov, c), Palsa (Iškoras, e) and Mire (Iškoras, f). Maximum annual ALT (dashed) and maximum annual surface water height (solid) are shown. Subsidence due to ice loss is shown by a deepening of the surface (d).

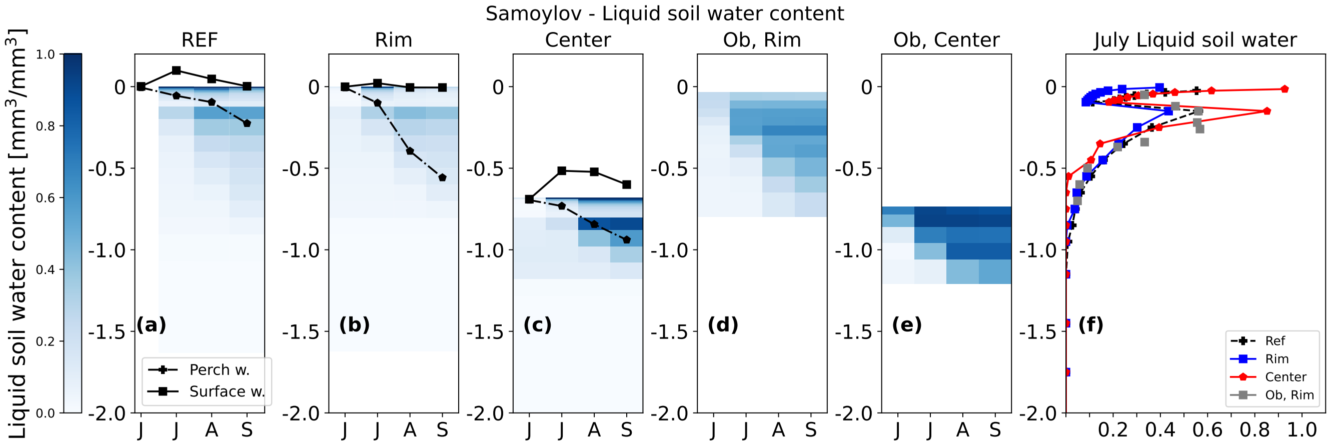

Figure 5. Mean monthly liquid soil water content in Samoylov for REF (a), Rim (b), Center (c) compared to observations for Rim (d) and Center (e). Observations are only available until $0.7\,\mathrm{m}$ depth. Only months with liquid soil water (summer) are shown. Dashed lines show the perched water table, and solid black lines surface water. Panel f shows July liquid soil water content at different depths.

water is distributed over a larger modeling area. A perched water table develops in all tiles in the summer, deepening rapidly at the Mire and REF with ALT.

3.4 Excess ice

Thawing of excess ground ice leads to ground subsidence. At Iškoras, REF shows $19\,\%$ ice loss after 1995 and $0.27\,\mathrm{m}$ of subsidence (Fig. 3). In contrast, tiling maintains Palsa stability: the Mire experiences substantial ALT deepening after 1990 but contains no excess ice, and the Palsa shows no ice loss. Late-simulation warming suggests the potential onset of Palsa degradation.

At Samoylov, subsidence and ice loss are minimal. REF shows $4\,\%$ ice loss and $0.04\,\mathrm{m}$ subsidence after 2005; the Rim loses $3\,\%$ and subsides $0.02\,\mathrm{m}$ after 2009. No change occurs at the Center. Early indicators of permafrost degradation are visible at Samoylov: ALT deepening and increasing soil temperatures (Section 3.2), both signs of emerging instability.

3.5 Fluxes

3.5.1 Heat fluxes

Soil temperatures are strongly connected to surface energy partitioning, and the soil conditions described above are reflected in the summer heat flux patterns. Figure 6 shows mean summer heat fluxes for 2004-2014.

At Iškoras (Fig. 6 top), summer heat fluxes exceed those at Samoylov, primarily due to a longer summer season and warmer temperatures. SH is much higher at the dry, elevated Palsa ($137\,\mathrm{W\,m^2}$) than in the wet Mire ($19\,\mathrm{W\,m^2}$). Conversely, LH at the Mire ($208\,\mathrm{W\,m^2}$) and REF ($197\,\mathrm{W\,m^2}$) far exceeds that at the Palsa. This reflects saturation at the Mire and REF, where

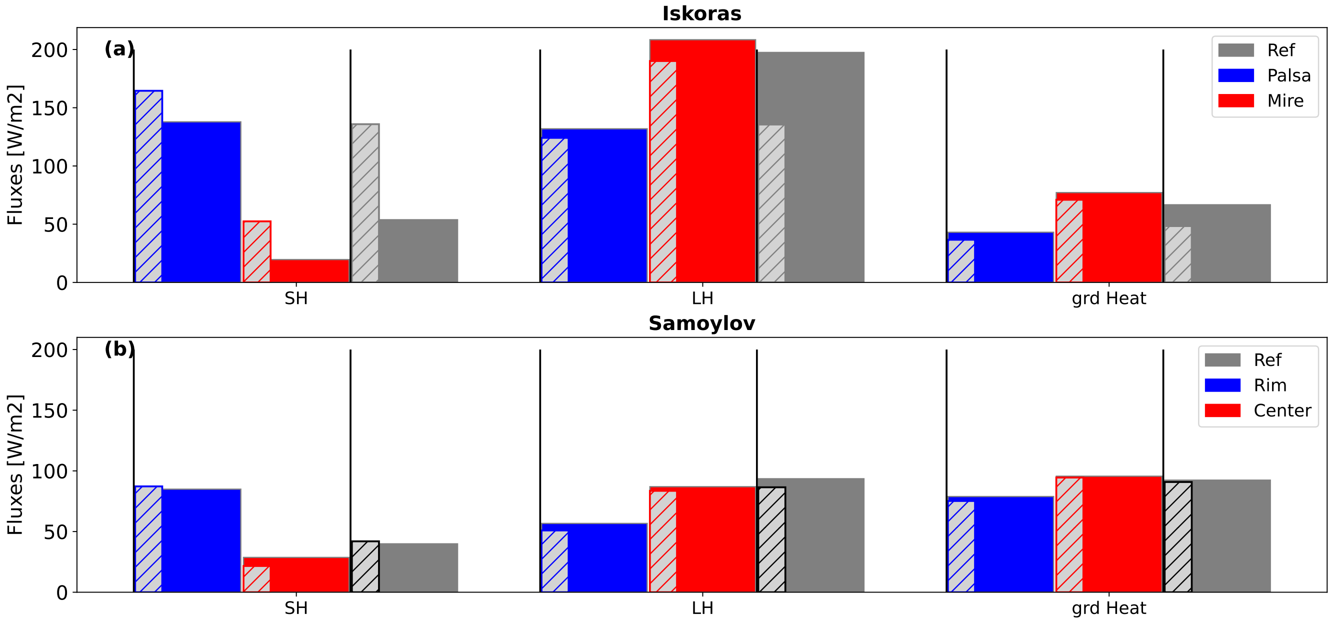

Figure 6. Mean summer (JJA) heat fluxes (2004-2014) for Iškoras (a) and Samoylov (b), Sensible heat (SH), Latent heat (LH) and ground heat fluxes (grd heat) are shown for Palsa/Rim (blue) Mire/Center (red) and REF (gray), Fluxes for period 1910-1920 are included for comparison (patterned part of the bars).

most available energy is consumed by phase change. In REF and to some extent at the Mire, rapid active-layer deepening and excess-ice melt further enhance LH. Ground heat flux is largest at the Mire, partly due to greater energy input during snowmelt.

Since 1910, summer heat fluxes at Iškoras have changed substantially, indicating system instability. In REF, SH decreased by roughly 60 % and LH increased by 27 %, primarily due to excess-ice melting and reduced annual temperature amplitude. Similar but weaker trends occur at the Palsa and Mire. At the Mire, the LH increase is mainly associated with rising soil saturation. The ground heat increases slightly for all simulations.

At the Polygon site in Samoylov (bottom panel), the sensible heat flux (SH) at the Rim (84 $\mathrm{W\,m^2}$) is more than twice that of the Center (28 $\mathrm{W\,m^2}$). SH at the Center and REF (39 $\mathrm{W\,m^2}$) is similar. The enhanced SH at the Rim reflects its larger annual soil temperature amplitude. Latent heat flux (LH) is highest in REF (93 $\mathrm{W\,m^2}$). LH at the Center (86 $\mathrm{W\,m^2}$) exceeds that at the Rim (56 $\mathrm{W\,m^2}$), because saturated soils at the Center and in REF allocate a large fraction of available energy to phase change during spring and autumn. The ground heat flux is comparable for all three simulations.

In the tiled simulations, the summer energy budget is dominated by LH, accounting for 50 % of the total energy (340 $\mathrm{W\,m^2}$), followed by SH (approximately 30 %) and ground heat flux (20 %). This partitioning agrees with observations from Samoylov (Langer et al., 2011a). Heat fluxes changed little between 1910-1020 and 2004-2014 (patterned parts in Fig. 6 show mean fluxes for 1910-1920), except for a slight increase in LH and ground heat flux, consistent with the relative thermal stability at Samoylov during the 20th century.

3.5.2 Soil water flux

Figure 7 shows mean annual water fluxes for 1960-2014. Incoming fluxes consist of rain (not shown) and snow. Outgoing fluxes include vegetation evapotranspiration, soil evapotranspiration, and surface runoff (including runoff from standing surface water). In the tiling configuration, lateral water exchange between tiles may be either incoming or outgoing, depending on season and hydraulic gradients. Liquid precipitation is identical across simulations, whereas snowfall differed due to redistribution (see Section 3.1). Even thought not using the biogeochemical module, tiles are still covered with plants, and basic variables like total leaf area index are calculated, leading to differences in vegetation evaporation.

At Samoylov, vegetation evaporation is low, but the Rim exhibits roughly twice the vegetation evapotranspiration of the Center. Soil evapotranspiration exceeds vegetation evapotranspiration in all simulations and is approximately 1.5 times larger at the Center than at the Rim.

Surface runoff is the dominant outgoing flux at Samoylov and shows the largest inter-annual variability. It is greatest at the Center -more than twice that of the Rim and REF- because the Center receives more snow, which contributes to surface runoff during snow melt. At the Rim and in REF, surface runoff is comparable in magnitude to soil evapotranspiration. At the Center, the largest runoff component is outflow from surface water (surface water outflow). This flux is negligible at the Rim and in REF, where surface water is absent, but substantial at the Center, where surface water persists through most of the snow-free season. Saturated soils at the Center limit infiltration and further enhance surface outflow. Outgoing fluxes at the Rim are smaller due to lower snow input and drier soils. Lateral water exchange also contributes to drying at the Rim.

Although Samoylov remains relatively stable since 1910, mean annual fluxes show moderate changes (Table 3). Both liquid and solid precipitation have increased over the past century. Soil evapotranspiration increases slightly, likely reflecting soil warming. Surface runoff increases markedly across all simulations, primarily due to higher precipitation and, at the Center, enhanced surface overflow.

At Iškoras, soil evapotranspiration and surface runoff dominate the annual water balance. At the Palsa, vegetation and soil evapotranspiration are of similar magnitude. Evapotranspiration arises from vegetation as well as from exposed soil or snow surfaces, which are common there. In contrast, evapotranspiration at the Mire exceeds that at the Palsa, because saturated or water covered surfaces enhance evaporation while limiting vegetation growth. Surface runoff at the Mire is much higher than at the Palsa and REF, primarily due to greater snowfall. At the Mire, surface water outflow further contributes, but is negligible at the Palsa. The lateral water flux enhances drying of the Palsa.

Water fluxes at Iškoras change substantially over the 20th century (Table 3), confirming local instability. Vegetation evapotranspiration decreases at all sites, most strongly at the Mire, due to expanding surface water coverage. Soil evapotranspiration increases markedly at the Mire and in REF, while remaining nearly unchanged at the Palsa. In REF, the collapse of the Palsa-like structure leads to soil saturation and pond formation, which, together with warming, enhances soil evaporation. Surface runoff increases at all tiles. At the Palsa, the increase is mainly driven by rising precipitation; at the REF, it is additionally amplified by soil saturation. At the Mire, overflow from standing water increases from nearly zero to up to $85\,\mathrm{mm\,year^{-1}}$- significantly enhancing surface runoff. Lateral water flux between tiles also intensifies.

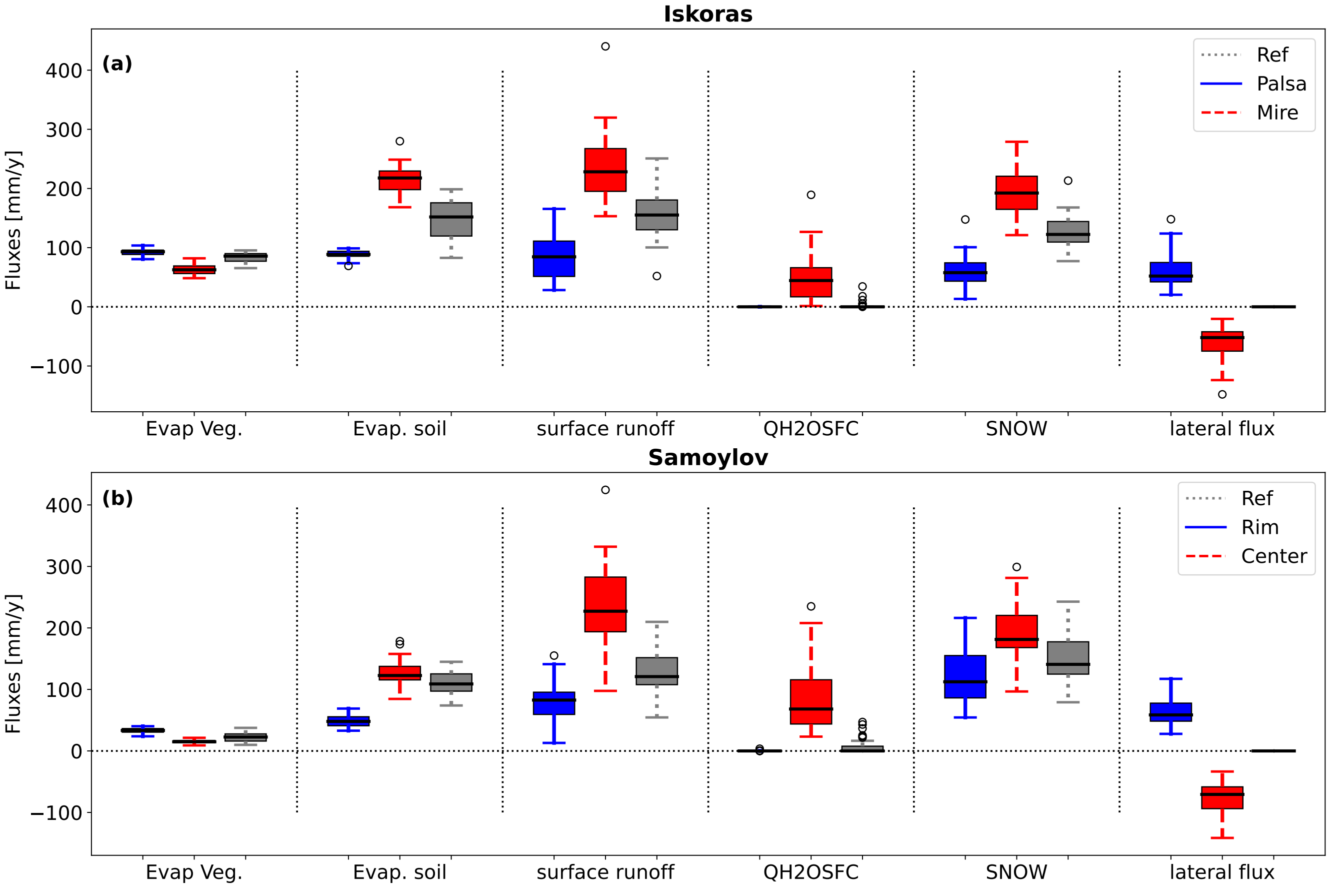

Figure 7. Mean yearly (1960-2014) incoming and outgoing water fluxes for Iškoras (a) and Samoylov (b) for Palsa (Rim), Mire (Center), and REF. Outgoing fluxes are Evap. veg (evaporation from vegetation), Evap. soil (evapotranspiration from soil) and surface runoff (including flux from standing surface water (QH2OSFC)). From the incoming fluxes only snow is shown. For the tiling approach lateral water flux is shown as well.

	year	Evaporation	Evapotranspiration	Surface runoff	surface water outflow	Lateral water flux	Rain+Snow
Samoylov							
Rim	1910-1920	34.68	42.18	47.92	0.0	53.5	202.20
	2004-2014	34.37	49.4	92.3	0.05	66.15	241.19
Center	1910-1920	15.13	131.48	170.2	53.29	-64.57	306.88
	2004 -2014	15.42	138.93	237.54,	81.63	-79.84	209.83
REF	1910 -1920	24.72	104.65	82.17	0.52	-	249.63
	2000 -2014	22.54	121.92	128.23	5.66	-	272.29
Iškoras							
Palsa	1910 -1920	92.77	82.74	25.3	0.0	9.48	266.56
	2004 -2014	91.85	88.61	90.73	0.0	79.27	354.12
Mire	1910-1920	78.49	159.3	135.93	1.83	9.48	410.63
	2004 -2014	60.62	225.03	275.43	84.36	-79.27	487.96
REF	1910-1920	92.88	89.6	105.31	0.0	-	228.59
	2004 -2014	77.6	177.8	159.01	7.11	-	421.01

Table 3. Mean annual water fluxes for Iškoras and Samoylov for 1910-1920 and 2004-2014. Fluxes for evaporation from vegetation, soil evapotranspiration, surface runoff (including flux from standing surface water (surface water outflow)), and lateral flux between the tiles are shown. Incoming water (rain and snow) is added for comparison. For the REF no lateral fluxes are calculated. All fluxes are in $\mathrm{mm\,year^{-1}}$.

3.6 Sensitivity analysis

3.6.1 Soil temperature and Subsidence

Figure 8 shows simulated Palsa elevation at Iškoras for the sensitivity experiments.

Palsa stability strongly depends on process configuration. Only simulations that include snow redistribution (+S, +SW, +SH, and fully coupled) maintain stable Palsa elevation. These are also the only experiments in which Palsa soil temperatures at $0.25\,\mathrm{m}$ remain below $0\,^{\circ}\mathrm{C}$ (Table 4). The fully coupled simulation produces the highest Palsa temperature among the stable cases, whereas disabling individual lateral fluxes tends to enhance cooling. Activating snow redistribution alone (+S) produces the largest temperature contrast between Palsa and Mire, emphasizing the dominant role of snow.

Simulations without lateral fluxes (no flux), and with only lateral heat flux (+H), show Palsa degradation beginning in the 1940s, followed by rapid excess ice thaw and associated subsidence after 2000. Thaw rates are comparable to REF but begin earlier. The +H experiment also produces the warmest Palsa temperature and minimal tile contrast. Experiments including only lateral water flux (+W) or disabling snow (+WH) produce behavior similar to REF.

At Samoylov, none of the simulations exhibit substantial subsidence, reflecting climatic conditions, which are, despite significant warming (Section 3.2), still cold enough to preserve permafrost and ground ice. Even in the warmest configuration (no flux), soil temperatures remain below thresholds for excess ice melt. However, marked differences in $0.25\,\mathrm{m}$ soil temperatures occur (Table 4), with Rim temperatures consistently lower than Center temperatures.

Snow redistribution exerts the strongest control. Enabling only snow redistribution (+S) decreases Rim soil temperature by more than 3°C and increases Center soil temperature by $1.1°$C relative to REF, producing the largest temperature contrast. Disabling snow redistribution yields the smallest Rim-Center difference ($0.4°$C). Lateral heat flux alone has minimal impact. Disabling heat flux (+SW) produces results similar to +S, indicating that lateral water flux alone has minimal thermal influence. Disabling lateral water flux yields results close to the fully coupled simulation.

Overall, snow redistribution dominates thermal dynamics, while lateral heat and water exchange moderate extreme contrasts.

3.6.2 Lateral heat and water flux

Lateral heat and water flux exhibit distinct seasonal patterns and magnitudes depending on site configuration (Section 3.5).

At Iškoras, lateral heat flux is strongest in the fully coupled simulation and in the experiment combining heat exchange and snow redistribution (+ SH). Fluxes peak during snowmelt (April and May), when temperature gradients between tiles are large. Substantial heat exchange persists into summer, because Palsa soils at $0.68\,\mathrm{m}$ remain cold, while Mire surface temperatures are warm. Without snow redistribution (+ H, + WH), lateral heat exchange is weak and occurs mainly in later summer and autumn, when elevation differences result in delayed Palsa cooling.

Lateral water flux peaks during snowmelt and again in September, when ALT depth is maximal and soils approach saturation. The largest instantaneous fluxes occur when only water exchange is enabled (+ W). Although annual means are small, this configuration produces flow from the Palsa to the Mire during snowmelt and reverse flow in autumn when hydraulic gradients invert. In +WH and +SW simulations, lateral water flux occurs primarily from the Palsa to the Mire during snowmelt and early refreezing.

At Samoylov, lateral heat flux is strongest in the fully coupled and +SH experiments, which generate the largest temperature contrast. Heat exchange peaks in winter and weakens in summer as soil temperatures between tiles converge. Lateral water fluxes occur during the frost free period, with flow from the Rim to the Center during early thaw and partial reversal during refreezing. Similar to Iškoras, the largest fluxes occur in +W, and the smallest in the fully coupled simulation.

4 Discussion and Conclusion

In this study, we present a tiling approach for modeling permafrost landscapes in CLM5 that enables simulations of rapid thawing events and landscape dynamics. To represent permafrost microtopography, the natural vegetated soil column is split into two interacting tiles that simulate distinct components of patterned permafrost landscapes, such as the Palsa and the Mire of a peat plateau. Lateral fluxes of water and heat between the tiles are incorporated, together with snow redistribution from the higher to the lower tile. Each tile is initialized with distinct soil profiles and excess ice content, allowing representation of contrasting landscape elements and their evolution. Apart from lateral exchange, soil physical processes are solved separately for each tile, providing a more realistic representation of landscape heterogeneity.

	REF	coupled	no flux	+ S	+ H	+ W	+ WH	+ SW	+ SH
Samoylov									
Rim	-6.40	-8.62	-6.4	-9.82	-6.62	-6.75	-7.15	-9.52	-8.73
Center	-	-7.06	-7.81	-5.30	-7.33	-7.88	-7.62	-5.0	-7.17
Iškoras									
Palsa	-	-0.54	2.07	-1.45	2.00	1.46	1.63	-1.47	-0.67
Mire	2.07	2.38	1.97	3.02	1.95	1.78	1.69	3.02	2.52

Table 4. Mean annual soil temperature (2010-2014) at $0.25\,\mathrm{m}$ soil depths at Samoylov and Iškoras for the sensitivity study. Temperatures are in °C. For experiment explanation see Table 2.

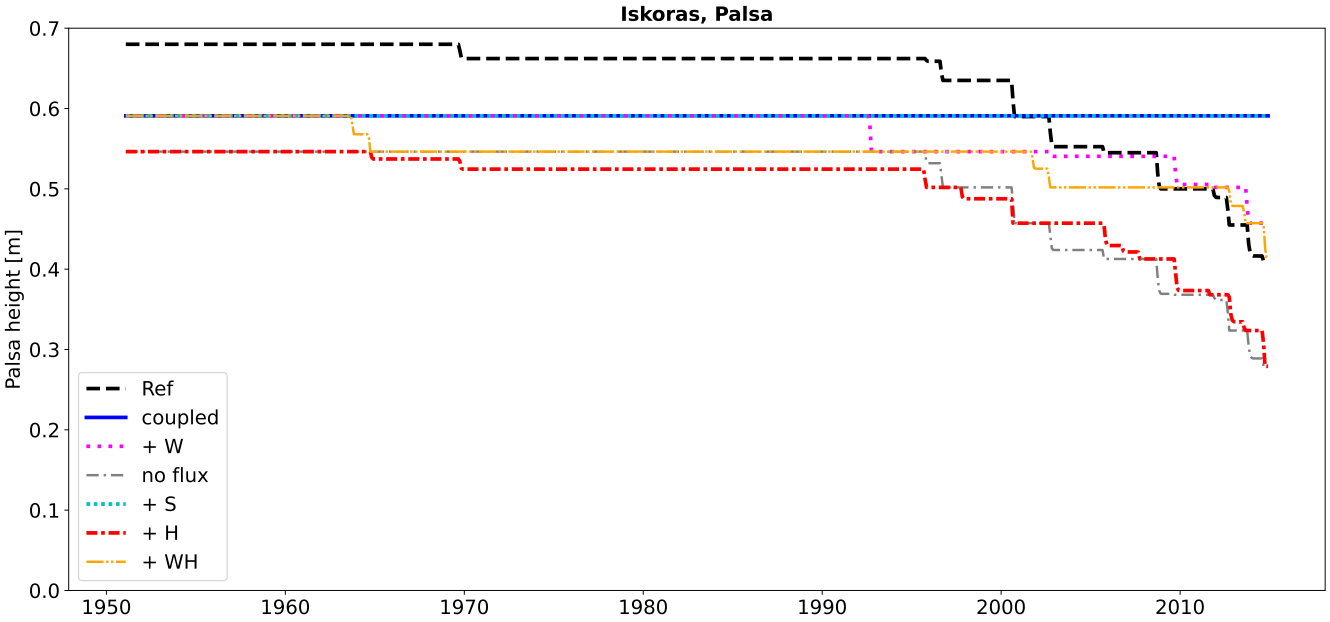

Figure 8. Elevation of the Palsa in Iškoras for REF (Ref, black, dashed) and standard tiling (coupled, blue, solid). Simulations are compared to experiments from the sensitivity study with just one process switched on; +S, +H, +W, see Table 2. Additionally, the simulation with + WH is shown. Simulations + SW and + SH are missing, because they show the same pattern as coupled.

https://doi.org/10.5194/egusphere-2026-1039
Preprint. Discussion started: 30 April 2026

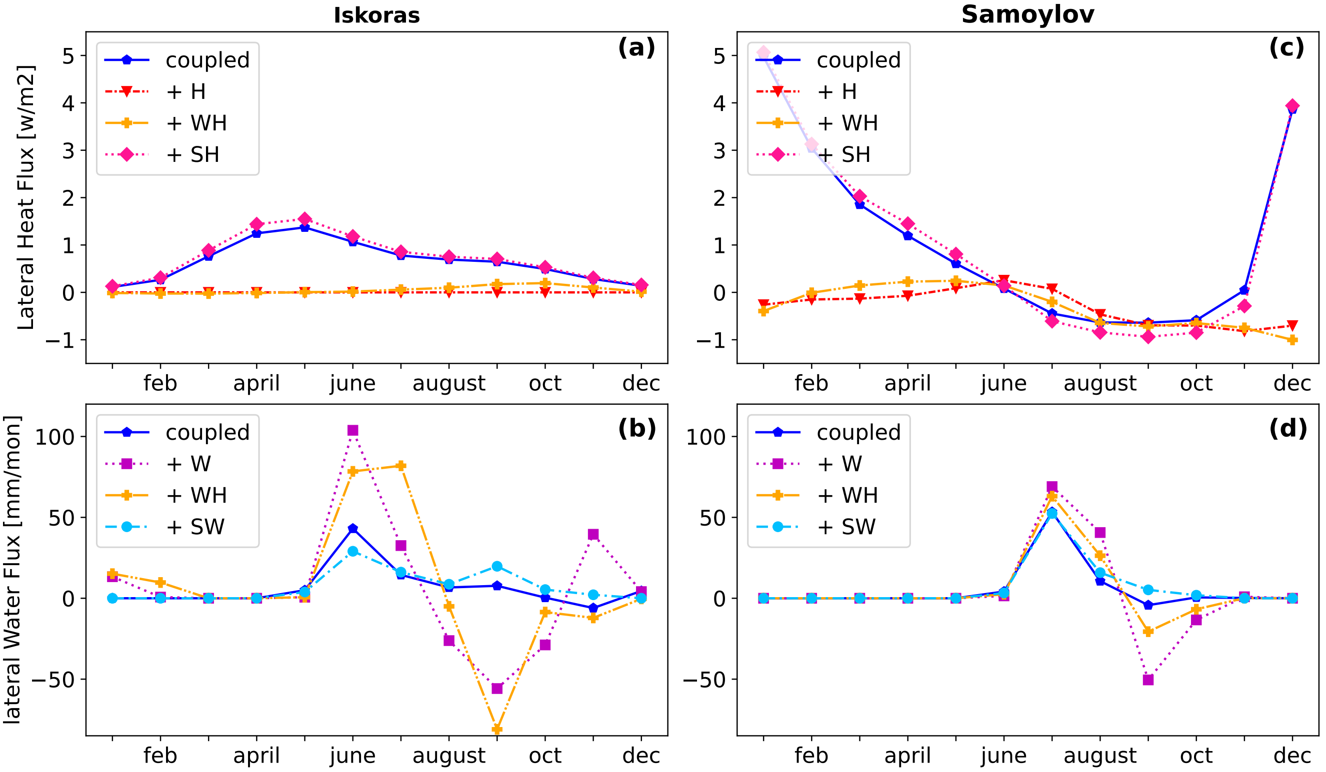

Figure 9. Lateral heat flux (a, c) and lateral water flux (b, d) for Iškoras (left) and Samoylov (right). Mean monthly fluxes for 2004-2014 are shown. Only simulations with lateral fluxes are shown. For experiment explanation see Table 2.

The model is evaluated at two contrasting sites: a peat plateau in northern Norway (Iškoras) and a polygonal tundra landscape in northeast Siberia, Russia (Samoylov). Performance is assessed relative to the standard CLM5 configuration, with emphasis on soil thermal and hydrological processes.

The new implementation substantially improves the representation of permafrost landscapes with respect to soil physics. By including key subgrid processes, it captures landscape heterogeneity and dynamics. The model successfully simulates contrasting landscape components: a drier, colder elevated tile (Palsa/Rim) and a wetter, warmer, lower tile (Mire/Center). Similar improvements have been reported in other land surface models using tiling approaches (Aas et al., 2019; Nitzbon et al., 2021), supporting tiling as a robust strategy to represent multiscale heterogeneity. While Cai et al. (2020) used duplicated landscape columns in CLM to investigate varying excess ice content, the presented approach extends this framework by explicitly coupling tiles through lateral fluxes of snow, heat, and water and by allowing differences in both soil structure and ice content. This enables the simulation of interacting landscape units rather than independent column experiments.

At the Palsa site, tiling is essential for reproducing the observed landscape state. In standard CLM5, the Palsa begins to thaw in the 1980s (Fig. 3), while the tiling configuration maintains stable Palsas until 2014, consistent with field observations.

https://doi.org/10.5194/egusphere-2026-1039
Preprint. Discussion started: 30 April 2026

Although direct ALT measurements are unavailable for comparison, modeled ALT differences between tiles suggest a more realistic representation than REF: while the Palsa maintains ALT below 1 m, ALT at the Mire is much deeper. In reality, there should not be any permafrost at the Mire. The remaining permafrost in the simulations is likely due to too cold air temperature in the forcing data, taken from the Karasjok station, and an overestimation of peat insulation. Such spatial contrasts cannot be represented in standard CLM5 but are critical for long-term projections of thaw trajectories and landscape evolution.

Simulating soil temperatures remains challenging at both sites. At Samoylov, deep annual mean soil temperatures agree well with observations and improve by approximately 2°C, relative to standard CLM. This improvement is relevant because deep soil temperatures and changes in the depth of zero annual amplitude are a key indicator of permafrost warming (Biskaborn, 2019). Reproducing the observed surface soil temperature and the annual cycle remains challenging at both sites. Summer surface temperatures are overestimated, likely due to overly dry soils (reducing thermal conductivity), uncertainties in atmospheric forcing, and simplified vegetation shading. At Iškoras, winter soil temperatures at the Palsa are too low, possibly reflecting insufficient snow insulation, bias in snow density, or overestimated thermal conductivity of frozen peat. Similar biases in frozen soil thermal conductivity have been documented for CLM5 in permafrost soils at the Tibet plateau (Yang et al., 2021). Sensitivity tests indicate that increasing the snow-redistribution threshold, thereby enhancing early-winter snow cover, raises winter soil temperature. At Samoylov, winter temperatures are too warm, primarily due to excessive winter snowfall, which is attributed to uncertainties in the forcing data. Reducing winter precipitation by 50 % improves winter soil temperature but leads to an underestimation of deep soil temperature. Those simulations also underestimate soil moisture due to too low annual precipitation. In autumn, modeled soil temperatures decrease too rapidly relative to observations, likely due to insufficient water content in the soil. Rapid soil freezing increases effective soil thermal conductivity and enhances conductive cooling.

Despite these limitations, the tiling implementation clearly improves representation of the contrasting soil thermal regime relative to standard CLM5.

Snow redistribution emerges as the dominant control on both present-day conditions and long-term evolution. It strongly influences winter soil temperature and soil moisture, consistent with the well-established insulating effect of snow (Zhang, 2005). Small-scale snow cover differences can alter soil temperatures by several degrees and are known for their crucial effect on Palsa development and ice-wedge formation. Representing subgrid snow contrast is therefore essential. The tiling framework enables simulation of distinct snow regimes (thin, wind-blown snow on elevated tiles and deeper snow on lower tiles) without substantially increasing computational cost or requiring higher spatial resolution.

The introduced lateral fluxes between tiles significantly improve the representation of soil physical conditions. They work as a governing source to mitigate effects introduced by snow redistribution. Lateral heat flux scales with soil temperature gradients and peaks when inter-tile contrasts are strongest- primarily in winter at Samoylov and during snowmelt and summer at Iškoras. The larger elevation differences at Iškoras (65 cm) enhance vertical and lateral thermal gradients, particularly during summer, when Mire surface soils warm while Palsa soils remain cold (compare Fig. 2 f and g). In contrast, lateral heat fluxes at Samoylov are generally stronger due to larger winter temperature contrast between tiles. Lateral heat fluxes lead to less pronounced inter-tile temperature differences in winter in Samoylov and in summer in Iškoras. Lateral water fluxes occur only during the thawed period and are governed by differences in perched water-table height. Fluxes are larger at Iškoras than at

Samoylov because (i) active-layer depth is greater, allowing more soil layers to participate in the flux, and (ii) soil-moisture contrasts between the tiles are more pronounced. Lateral water fluxes lead to soil drying of the higher tile in summer.

A major improvement of the new implementation lies in the modeling of soil hydrology. Observed soil hydrological patterns are reproduced well. Standard CLM can simulate only a single soil-moisture regime per grid cell, whereas the tiling approach reproduces two coexisting regimes: a saturated lower tile with seasonal pounding and a drier elevated tile. Soil hydrology is particularly relevant for modeling greenhouse gas fluxes. Soil wetness and inundation influence the balance between carbon dioxide and methane emissions and determine whether decomposition proceeds under aerobic or anaerobic conditions. Accurate representation of soil moisture and surface water therefore directly affects estimates of carbon turnover and methane production. The achieved improvements in soil hydrology give a strong basis for biogeochemical modeling in the future.

Overall, the new implementation explicitly represents excess-ice melt, subsidence, and rapid thaw processes and substantially improves simulation of thermal and hydrological regimes in heterogeneous permafrost landscapes. These advances provide a physically consistent basis for future modeling runs with biogeochemical modules activated to assess present and future greenhouse gas emissions, including effects of pounding, inundation, and surface subsidence. Investigation of coupled carbon dynamics constitutes a logical next step but lies beyond the scope of the present study.

Code availability. The original Community Land Model is available through the Community Terrestrial System Model (CTSM) git repository (https://github.com/ESCOMP/CTSM). The source code of the specific model development of this study is accessible under the repository https://github.com/estherbe3/CTSM archived under DOI https://doi.org/10.5281/zenodo.18787515 (Bender, Esther, 2026).

Appendix A

Author contributions. EB did the model development work and wrote the initial draft. MD, KSA help with the model development and provided ideas. HL initialized the study provided ideas and help with the study design, SW, FL and SZ gave value input to improve, study design and paper draft.

Competing interests. The contact authors declared that none of the authors has any competing interests.

Acknowledgements. EB, HL, KA, SW were supported by the research Council of Norway project (328922). AI tools were used to help with grammar and spelling of the english language

https://doi.org/10.5194/egusphere-2026-1039
Preprint. Discussion started: 30 April 2026

Depth [m]	Sand tile[%] 1	Clay tile 1 [%]	Organic tile1 [kg/m^3]	Sand Tile2 [%]	Clay tile 2 [%]	Organic Tile 2 [kg/m^3
Iškoras						
0.00-0.10	50	20	130	50	20	130
0.1-0.25	50	12	130	50	12	130
0.25-1.5	50	12	130	70	40	90
1.5 >	50	12	0	70	12	0
Samoylov						
0.00-0.09	36	15	130	36	15	130
0.1-0.25	60	20	130	36	15	130
0.25-0.5	60	20	40	40	40	130
0.5-1.25	60	20	40	40	40	90
1.25 >	60	20	0	40	40	0

Table A1. Soil structure for Iškoras and Samoylov. Amounts of clay and Sand are in % Organic is $\mathrm{kg\,m^{-1}}$

	REF	fl coupled	no flux	+ S	+ H	+ W	+ WH	+ SW	+ SH
Samoylov									
Rim	0.55	0.45	0.55	0.53	0.56	0.49	0.46	0.41	0.53
Center	-	0.79	0.80	0.87	0.83	0.75	0.82	0.86	0.82
Iškoras									
Palsa	-	0.57	0.84	0.63	0.85	0.64	0.71	0.57	0.61
Mire	0.84	0.85	0.74	0.54	0.74	0.79	0.72	0.53	0.82

Table A2. Mean July volumetric soil water content(2010-2014) at 25 cm soil depths at Samoylov and Iškoras for the sensitivity study

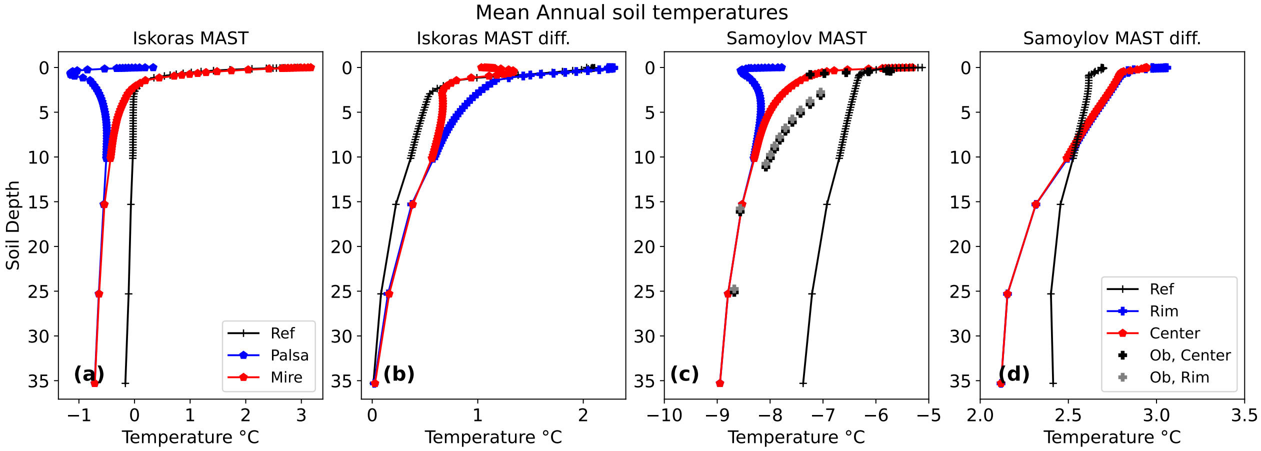

Figure A1. Mean annual soil temperature from 2002-2014 for Iškoras (a) and Samoylov (c) as well as differences in soil temperature from 2004-2004 to 1910 to 1920. For Samoylov observations are also shown.

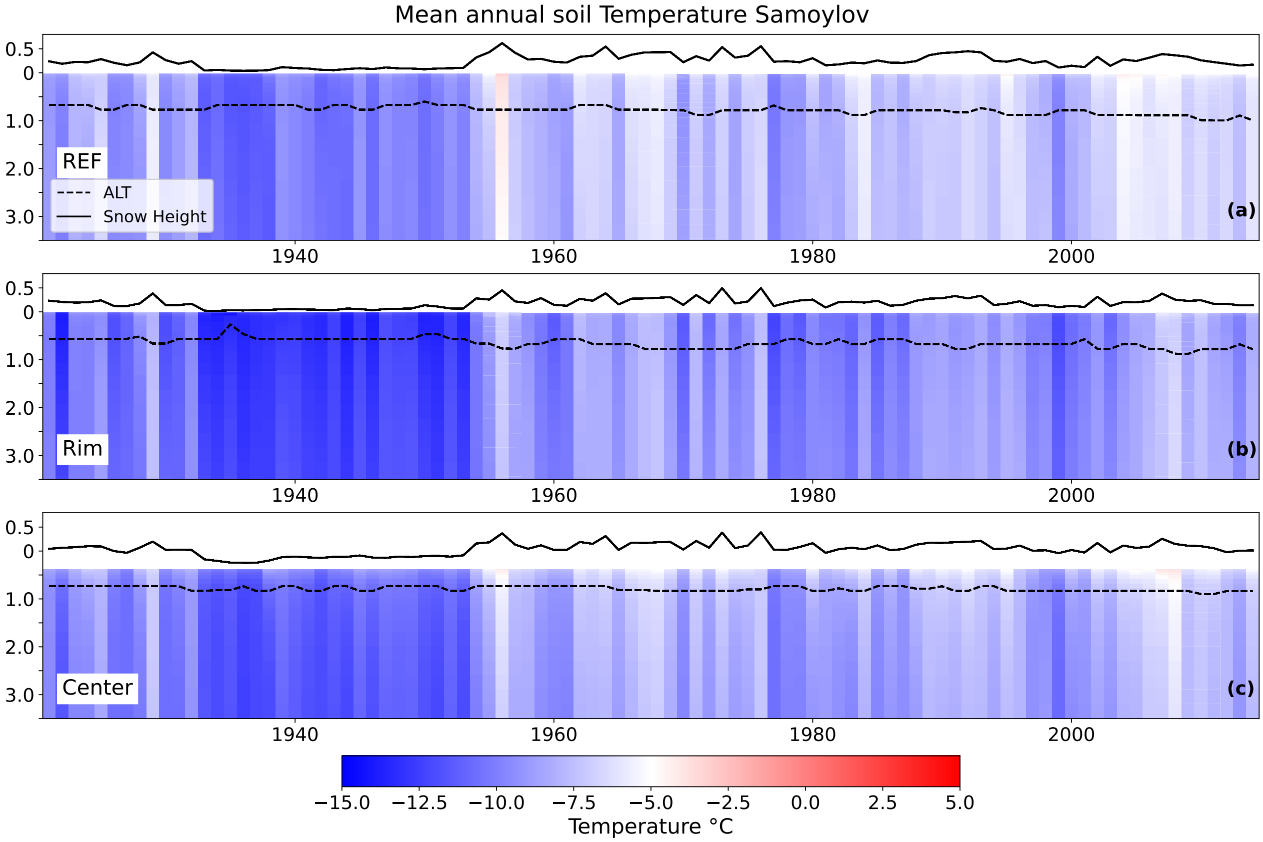

Figure A2. Mean annual soil temperature at Samoylov from 1930-2024 for Ref (a), Rim (b) and Center(c), maximum annual snow height (solid line) and ALT (dashed line) are shown as black lines.

Financial support. FL and JZ are co-supported by the National Key Research and Development Program of China (grant no. 2022YFE0106500)

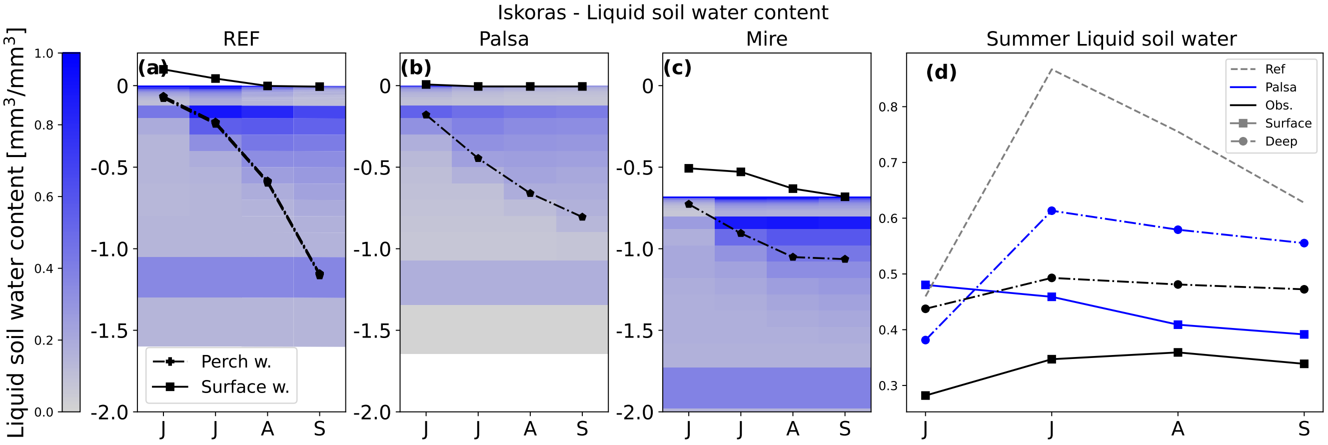

Figure A3. Mean monthly values for liquid soil water content at Iškoras. For Ref (a), Palsa (b) and Mire (c). Perch water table(dotted) and Surface water (solid) are shown in black lines. The plot on the right shows values for Palsa for the first 30 cm and deeper in the soil compared to observations. Values for the Mire are not shown as observation and simulation are nearly saturated in the Summer.

575 **References**

https://doi.org/10.5194/egusphere-2026-1039
Preprint. Discussion started: 30 April 2026

References

Aas, K. S., Martin, L., Nitzbon, J., Langer, M., Boike, J., Lee, H., Berntsen, T. K., and Westermann, S.: Thaw processes in ice-rich permafrost landscapes represented with laterally coupled tiles in a land surface model, The Cryosphere, 13, 591–609, https://doi.org/10.5194/tc-13-591-2019, publisher: Copernicus GmbH, 2019.

Andresen, C. G., Lawrence, D. M., Wilson, C. J., McGuire, A. D., Koven, C., Schaefer, K., Jafarov, E., Peng, S., Chen, X., Gouttevin, I., Burke, E., Chadburn, S., Ji, D., Chen, G., Hayes, D., and Zhang, W.: Soil moisture and hydrology projections of the permafrost region – a model intercomparison, The Cryosphere, 14, 445–459, https://doi.org/10.5194/tc-14-445-2020, publisher: Copernicus GmbH, 2020.

Bender, Esther: estherbe3/CTSM: Tiling_code_final (Zenodo), https://doi.org/10.5281/zenodo.18787515, 2026.

Biskaborn, B. K. e.: Permafrost is warming at a global scale, Nature communications, 10, 1–11, 2019.

Boike, J., Kattenstroth, B., Abramova, K., Bornemann, N., Chetverova, A., Fedorova, I., Frob, K., and Grigoriev, M.: Baseline characteristics of climate, permafrost and land cover from a new permafrost observatory in the Lena River Delta, Siberia (1998–2011), european geosciences journal, 2013.

Boike, J., Nitzbon, J., Anders, K., Grigoriev, M., Bolshiyanov, D., Langer, M., Lange, S., Bornemann, N., Morgenstern, A., Schreiber, P., Wille, C., Chadburn, S., Gouttevin, I., Burke, E., and Kutzbach, L.: A 16-year record (2002–2017) of permafrost, active-layer, and meteorological conditions at the Samoylov Island Arctic permafrost research site, Lena River delta, northern Siberia: an opportunity to validate remote-sensing data and land surface, snow, and permafrost models, Earth System Science Data, 11, 261–299, https://doi.org/10.5194/essd-11-261-2019, publisher: Copernicus GmbH, 2019.

Boike, J., Bolshiyanov, D. Y., Bornemann, N., Grigoriev, M. N., Grünberg, I., and Miesner, F.: Meteorologic data at station Samoylov (2020), PANGAEA, https://doi.org/10.1594/PANGAEA.949116, in: Boike, Julia; Cable, William L; Bolshiyanov, Dimitry Yu; Bornemann, Niko; Grigoriev, Mikhail N; Grünberg, Inge; Miesner, Frederieke (2022): Continuous measurements in soil and air at the permafrost long-term observatory at Samoylov Station (2002 et seq) [dataset bundled publication]. Alfred Wegener Institute - Research Unit Potsdam, PANGAEA, https://doi.org/10.1594/PANGAEA.947032, 2022.

Borge, A. F., Westermann, S., Solheim, I., and Etzelmüller, B.: Strong degradation of palsas and peat plateaus in northern Norway during the last 60 years, The Cryosphere, 11, 1–16, https://doi.org/10.5194/tc-11-1-2017, 2017.

Brown, J., Ferrians, O., Heginbottom, J., and Melnikov, E. S.: Circum-Arctic map of permafrost and ground-ice conditions, dataset, 1997.

Burke, E. J., Zhang, Y., and Krinner, G.: Evaluating permafrost physics in the Coupled Model Intercomparison Project 6 (CMIP6) models and their sensitivity to climate change, The Cryosphere, 14, 3155–3174, https://doi.org/10.5194/tc-14-3155-2020, publisher: Copernicus GmbH, 2020.

Cai, L., Lee, H., Aas, K. S., and Westermann, S.: Projecting circum-Arctic excess-ground-ice melt with a sub-grid representation in the Community Land Model, The Cryosphere, 14, 4611–4626, https://doi.org/10.5194/tc-14-4611-2020, publisher: Copernicus GmbH, 2020.

Chadburn, S. E., Krinner, G., Porada, P., Bartsch, A., Beer, C., Belelli Marchesini, L., Boike, J., Ekici, A., Elberling, B., Friborg, T., Hugelius, G., Johansson, M., Kuhry, P., Kutzbach, L., Langer, M., Lund, M., Parmentier, F.-J. W., Peng, S., Van Huissteden, K., Wang, T., Westermann, S., Zhu, D., and Burke, E. J.: Carbon stocks and fluxes in the high latitudes: using site-level data to evaluate Earth system models, Biogeosciences, 14, 5143–5169, https://doi.org/10.5194/bg-14-5143-2017, publisher: Copernicus GmbH, 2017.

Chadburn, S. E., Burke, E. J., Gallego-Sala, A. V., Smith, N. D., Bret-Harte, M. S., Charman, D. J., Drewer, J., Edgar, C. W., Euskirchen, E. S., Fortuniak, K., Gao, Y., Nakhavali, M., Pawlak, W., Schuur, E. A. G., and Westermann, S.: A new approach to simulate peat accumulation, degradation and stability in a global land surface scheme (JULES vn5.8_accumulate_soil) for northern and temperate peatlands, Geoscientific Model Development, 15, 1633–1657, https://doi.org/10.5194/gmd-15-1633-2022, publisher: Copernicus GmbH, 2022.

Dirmeyer, P. A., Gao, X., Zhao, M., Guo, Z., Oki, T., and Hanasaki, N.: GSWP-2: Multimodel Analysis and Implications for Our Perception of the Land Surface, Bulletin of the American Meteorological Society, 87, 1381 – 1398, https://doi.org/10.1175/BAMS-87-10-1381, 2006.

Ekici, A., Lee, H., Lawrence, D. M., Swenson, S. C., and Prigent, C.: Ground subsidence effects on simulating dynamic high-latitude surface inundation under permafrost thaw using CLM5, Geoscientific Model Development, 12, 5291–5300, https://doi.org/10.5194/gmd-12-5291-2019, publisher: Copernicus GmbH, 2019.

Farquharson, L. M., Romanovsky, V. E., Cable, W. L., Walker, D. A., Kokelj, S. V., and Nicolsky, D.: Climate Change Drives Widespread and Rapid Thermokarst Development in Very Cold Permafrost in the Canadian High Arctic, Geophysical Research Letters, 46, 6681–6689, https://doi.org/10.1029/2019GL082187, _eprint: https://agupubs.onlinelibrary.wiley.com/doi/pdf/10.1029/2019GL082187, 2019.

Fritz, M., Wolter, J., Rudaya, N., Palagushkina, O., Nazarova, L., Obu, J., Rethemeyer, J., Lantuit, H., and Wetterich, S.: Holocene ice-wedge polygon development in northern Yukon permafrost peatlands (Canada), Quaternary Science Reviews, 147, 279–297, https://doi.org/10.1016/j.quascirev.2016.02.008, 2016.

Grosse, G., Jones, B., and Arp, C.: 8.21 Thermokarst Lakes, Drainage, and Drained Basins, in: Treatise on Geomorphology, edited by Shroder, J. F., pp. 325–353, Academic Press, San Diego, https://doi.org/https://doi.org/10.1016/B978-0-12-374739-6.00216-5, 2013.

Hugelius, G., Strauss, J., Zubrzycki, S., Harden, J. W., Schuur, E. A. G., Ping, C.-L., Schirrmeister, L., Grosse, G., Michaelson, G. J., Koven, C. D., O'Donnell, J. A., Elberling, B., Mishra, U., Camill, P., Yu, Z., Palmtag, J., and Kuhry, P.: Estimated stocks of circumpolar permafrost carbon with quantified uncertainty ranges and identified data gaps, Biogeosciences, 11, 6573–6593, https://doi.org/10.5194/bg-11-6573-2014, 2014.

Jiao, Y., Davie-Martin, C. L., Kramshøj, M., Christiansen, C. T., Lee, H., Althuizen, I. H. J., and Rinnan, R.: Volatile organic compound release across a permafrost-affected peatland, Geoderma, 430, 116 355, https://doi.org/10.1016/j.geoderma.2023.116355, 2023.

Knoblauch, C., Beer, C., Sosnin, A., Wagner, D., and Pfeiffer, E.-M.: Predicting long-term carbon mineralization and trace gas production from thawing permafrost of Northeast Siberia, Global Change Biology, 19, 1160–1172, https://doi.org/https://doi.org/10.1111/gcb.12116, 2013.

Knoblauch, C., Beer, C., Liebner, S., Grigoriev, M., and Pfeiffer, E.: Methane production as key to the greenhouse gas budget of thawing permafrost, Nature Climate Change, https://doi.org/10.1038/s41558-018-0095-z, 2018.

Koven, C. D., Riley, W. J., and Stern, A.: Analysis of Permafrost Thermal Dynamics and Response to Climate Change in the CMIP5 Earth System Models, Journal of Climate, 26, 1877–1900, https://doi.org/10.1175/JCLI-D-12-00228.1, publisher: American Meteorological Society Section: Journal of Climate, 2013.

Langer, M., Westermann, S., Muster, S., Piel, K., and Boike, J.: The surface energy balance of a polygonal tundra site in northern Siberia – Part 1: Spring to fall, The Cryosphere, 5, 151–171, https://doi.org/10.5194/tc-5-151-2011, 2011a.

Langer, M., Westermann, S., Muster, S., Piel, K., and Boike, J.: The surface energy balance of a polygonal tundra site in northern Siberia – Part 2: Winter, The Cryosphere, 5, 509–524, https://doi.org/10.5194/tc-5-509-2011, 2011b.

Langer, M., Westermann, S., Boike, J., Kirillin, G., Grosse, G., Peng, S., and Krinner, G.: Rapid degradation of permafrost underneath waterbodies in tundra landscapes—Toward a representation of thermokarst in land surface models, Journal of Geophysical Research: Earth Surface, 121, 2446–2470, https://doi.org/https://doi.org/10.1002/2016JF003956, 2016.

Lawrence, D. M., Fisher, R. A., Koven, C. D., Oleson, K. W., Swenson, S. C., Bonan, G., Collier, N., Ghimire, B., van Kampenhout, L., Kennedy, D., Kluzek, E., Lawrence, P. J., Li, F., Li, H., Lombardozzi, D., Riley, W. J., Sacks, W. J., Shi, M., Vertenstein, M., Wieder, W. R., Xu, C., Ali, A. A., Badger, A. M., Bisht, G., van den Broeke, M., Brunke, M. A., Burns, S. P., Buzan, J., Clark, M., Craig, A., Dahlin, K., Drewniak, B., Fisher, J. B., Flanner, M., Fox, A. M., Gentine, P., Hoffman, F., Keppel-Aleks, G., Knox, R., Kumar, S., Lenaerts, J., Leung, L. R., Lipscomb, W. H., Lu, Y., Pandey, A., Pelletier, J. D., Perket, J., Randerson, J. T., Ricciuto, D. M., Sanderson, B. M., Slater, A., Subin, Z. M., Tang, J., Thomas, R. Q., Val Martin, M., and Zeng, X.: The Community Land Model Version 5: Description of New Features, Benchmarking, and Impact of Forcing Uncertainty, Journal of Advances in Modeling Earth Systems, 11, 4245–4287, https://doi.org/10.1029/2018MS001583, 2019.

Lee, H., Swenson, S. C., Slater, A. G., and Lawrence, D. M.: Effects of excess ground ice on projections of permafrost in a warming climate, Environmental Research Letters, 9, 124 006, https://doi.org/10.1088/1748-9326/9/12/124006, 2014.

Liljedahl, A. K., Boike, J., Daanen, R. P., Fedorov, A. N., Frost, G. V., Grosse, G., Hinzman, L. D., Iijma, Y., Jorgenson, J. C., Matveyeva, N., Necsoiu, M., Raynolds, M. K., Romanovsky, V. E., Schulla, J., Tape, K. D., Walker, D. A., Wilson, C. J., Yabuki, H., and Zona, D.: Pan-Arctic ice-wedge degradation in warming permafrost and its influence on tundra hydrology, Nature Geoscience, 9, 312–318, https://doi.org/10.1038/ngeo2674, publisher: Nature Publishing Group, 2016.

Martin, L. C. P., Nitzbon, J., Aas, K. S., Etzelmüller, B., Kristiansen, H., and Westermann, S.: Stability Conditions of Peat Plateaus and Palsas in Northern Norway, Journal of Geophysical Research: Earth Surface, 124, 705–719, https://doi.org/10.1029/2018JF004945, _eprint: https://onlinelibrary.wiley.com/doi/pdf/10.1029/2018JF004945, 2019.

Martin, L. C. P., Nitzbon, J., Scheer, J., Aas, K. S., Eiken, T., Langer, M., Filhol, S., Etzelmüller, B., and Westermann, S.: Lateral thermokarst patterns in permafrost peat plateaus in northern Norway, The Cryosphere, 15, 3423–3442, https://doi.org/10.5194/tc-15-3423-2021, publisher: Copernicus GmbH, 2021.

Matthes, H., Damseaux, A., Westermann, S., Beer, C., Boone, A., Burke, E., Decharme, B., Genet, H., Jafarov, E., Langer, M., Parmentier, F.-J., Porada, P., Gagne-Landmann, A., Huntzinger, D., Rogers, B. M., Schädel, C., Stacke, T., Wells, J., and Wieder, W. R.: Advances in Permafrost Representation: Biophysical Processes in Earth System Models and the Role of Offline Models, Permafrost and Periglacial Processes, 36, 302–318, https://doi.org/10.1002/ppp.2269, _eprint: https://onlinelibrary.wiley.com/doi/pdf/10.1002/ppp.2269, 2025.

Nitzbon, J., Langer, M., Westermann, S., Martin, L., Aas, K. S., and Boike, J.: Pathways of ice-wedge degradation in polygonal tundra under different hydrological conditions, The Cryosphere, 13, 1089–1123, https://doi.org/10.5194/tc-13-1089-2019, publisher: Copernicus GmbH, 2019.

Nitzbon, J., Westermann, S., Langer, M., Martin, L. C. P., Strauss, J., Laboor, S., and Boike, J.: Fast response of cold ice-rich permafrost in northeast Siberia to a warming climate, Nature Communications, 11, 2201, https://doi.org/10.1038/s41467-020-15725-8, number: 1 Publisher: Nature Publishing Group, 2020.

Nitzbon, J., Langer, M., Martin, L. C. P., Westermann, S., Schneider von Deimling, T., and Boike, J.: Effects of multi-scale heterogeneity on the simulated evolution of ice-rich permafrost lowlands under a warming climate, The Cryosphere, 15, 1399–1422, https://doi.org/10.5194/tc-15-1399-2021, publisher: Copernicus GmbH, 2021.

Norwegian Meteorological Institute: Air pressure at station level observations from weather station Karasjok, Finnmark, Norway (WIGOS ID: 0-20000-0-01065, station ID: 97251), https://data.met.no/dataset/a37662fe-d7a1-4601-919f-b7c8dfc3cf61, dataset, 2024.

Obu, J., Westermann, S., Bartsch, A., Berdnikov, N., Christiansen, H. H., Dashtseren, A., Delaloye, R., Elberling, B., Etzelmüller, B., Kholodov, A., Khomutov, A., Kääb, A., Leibman, M. O., Lewkowicz, A. G., Panda, S. K., Romanovsky, V., Way, R. G., Westergaard-Nielsen, A., Wu, T., Yamkhin, J., and Zou, D.: Northern Hemisphere permafrost map based on TTOP modelling for 2000–2016 at 1km2 scale, Earth-Science Reviews, 193, 299–316, https://doi.org/10.1016/j.earscirev.2019.04.023, 2019.

Olefeldt, D., Goswami, S., Grosse, G., Hayes, D., Hugelius, G., Kuhry, P., McGuire, A. D., Romanovsky, V. E., Sannel, A., Schuur, E., and Turetsky, M. R.: Circumpolar distribution and carbon storage of thermokarst landscapes, Nature Communications, 7, 13 043, https://doi.org/10.1038/ncomms13043, 2016.

Pirk, N., Aalstad, K., Mannerfelt, E. S., Clayer, F., de Wit, H., Christiansen, C. T., Althuizen, I., Lee, H., and Westermann, S.: Disaggregating the Carbon Exchange of Degrading Permafrost Peatlands Using Bayesian Deep Learning, Geophysical Research Letters, 51, e2024GL109 283, https://doi.org/10.1029/2024GL109283, _eprint: https://agupubs.onlinelibrary.wiley.com/doi/pdf/10.1029/2024GL109283, 2024.

Ran, Y., Li, X., Cheng, G., Che, J., Aalto, J., Karjalainen, O., Hjort, J., Luoto, M., Jin, H., Obu, J., Hori, M., Yu, Q., and Chang, X.: New high-resolution estimates of the permafrost thermal state and hydrothermal conditions over the Northern Hemisphere, Earth System Science Data, 14, 865–884, https://doi.org/10.5194/essd-14-865-2022, 2022.

Rantanen, M., Karpechko, A. Y., Lipponen, A., Nordling, K., Hyvärinen, O., Ruosteenoja, K., Vihma, T., and Laaksonen, A.: The Arctic has warmed nearly four times faster than the globe since 1979, Communications Earth & Environment, 3, 1–10, https://doi.org/10.1038/s43247-022-00498-3, number: 1 Publisher: Nature Publishing Group, 2022.

Runge, A., Nitze, I., and Grosse, G.: Remote sensing annual dynamics of rapid permafrost thaw disturbances with LandTrendr, Remote Sensing of Environment, 268, 112 752, https://doi.org/10.1016/j.rse.2021.112752, 2022.

Schuur, E., McGuire, A., and Schadel, C. e. a.: Climate change and the permafrost carbon feedback., Nature, 520, 171–179, 2015.

Schuur, E. A., Abbott, B. W., Commane, R., Ernakovich, J., Euskirchen, E., Hugelius, G., Grosse, G., Jones, M., Koven, C., Leshyk, V., Lawrence, D., Loranty, M. M., Mauritz, M., Olefeldt, D., Natali, S., Rodenhizer, H., Salmon, V., Schädel, C., Strauss, J., Treat, C., and Turetsky, M.: Permafrost and Climate Change: Carbon Cycle Feedbacks From the Warming Arctic, Annual Review of Environment and Resources, 47, 343–371, https://doi.org/10.1146/annurev-environ-012220-011847, 2022.

Seppälä, M.: Synthesis of studies of palsa formation underlining the importance of local environmental and physical characteristics, Quaternary Research, 75, 366–370, https://doi.org/10.1016/j.yqres.2010.09.007, publisher: Cambridge University Press, 2011.

Smith, N. D., Burke, E. J., Schanke Aas, K., Althuizen, I. H. J., Boike, J., Christiansen, C. T., Etzelmüller, B., Friborg, T., Lee, H., Rumbold, H., Turton, R. H., Westermann, S., and Chadburn, S. E.: Explicitly modelling microtopography in permafrost landscapes in a land surface model (JULES vn5.4_microtopography), Geoscientific Model Development, 15, 3603–3639, https://doi.org/10.5194/gmd-15-3603-2022, publisher: Copernicus GmbH, 2022.

Turetsky, M. R., Abbott, B. W., Jones, M. C., Walter Anthony, K., Olefeldt, D., Schuur, E. A. G., Koven, C., McGuire, A. D., Grosse, G., Kuhry, P., Hugelius, G., Lawrence, D. M., Gibson, C., and Sannel, A. B. K.: Permafrost collapse is accelerating carbon release, Nature, 569, 32–34, https://doi.org/10.1038/d41586-019-01313-4, 2019.

Vasiliev, A. A., Drozdov, D. S., Gravis, A. G., Malkova, G. V., Nyland, K. E., and Streletskiy, D. A.: Permafrost degradation in the Western Russian Arctic, Environmental Research Letters, 15, 045 001, https://doi.org/10.1088/1748-9326/ab6f12, 2020.

Westermann, S., Langer, M., Boike, J., Heikenfeld, M., Peter, M., Etzelmüller, B., and Krinner, G.: Simulating the thermal regime and thaw processes of ice-rich permafrost ground with the land-surface model CryoGrid 3, Geoscientific Model Development, 9, 523–546, https://doi.org/10.5194/gmd-9-523-2016, publisher: Copernicus GmbH, 2016.

725 Yang, S., Li, R., Wu, T., Wu, X., Zhao, L., Hu, G., Zhu, X., Du, Y., Xiao, Y., Zhang, Y., Ma, J., Du, E., Shi, J., and Qiao, Y.: Evaluation of soil thermal conductivity schemes incorporated into CLM5.0 in permafrost regions on the Tibetan Plateau, Geoderma, 401, 115 330, https://doi.org/https://doi.org/10.1016/j.geoderma.2021.115330, 2021.

Zhang, T.: Influence of the seasonal snow cover on the ground thermal regime: An overview, Reviews of Geophysics, 43, https://doi.org/10.1029/2004RG000157, _eprint: https://agupubs.onlinelibrary.wiley.com/doi/pdf/10.1029/2004RG000157, 2005.